

FRONTS AND PATTERNS
IN
REACTION-DIFFUSION EQUATIONS

by
Aric Arild Hagberg

A Dissertation Submitted to the Faculty of the
Graduate Interdisciplinary
Program in Applied Mathematics
In Partial Fulfillment of the Requirements
For the Degree of
Doctor of Philosophy
In the Graduate College
THE UNIVERSITY OF ARIZONA

1 9 9 4

Statement by Author

This dissertation has been submitted in partial fulfillment of requirements for an advanced degree at The University of Arizona and is deposited in the University Library to be made available to borrowers under rules of the library.

Brief quotations from this dissertation are allowable without special permission, provided that accurate acknowledgment of source is made. Requests for permission for extended quotation from or reproduction of this manuscript in whole or in part may be granted by the head of the major department or the Dean of the Graduate College when in his or her judgment the proposed use of the material is in the interests of scholarship. In all other instances, however, permission must be obtained from the author.

SIGNED: _____

Acknowledgments

Thanks to:

The Computational Science Graduate Fellowship Program of the Office of Scientific Computing in the Department of Energy, The Department of Education National Needs Fellowship, and The Center for Nonlinear Studies and Theoretical Division at Los Alamos National Laboratory for financial support.

Ehud Meron for landing in Tucson and providing scientific inspiration, guidance, and advice.

Mac Hyman, Dave Levermore, and **Bruce Bayly** for serving on my committee and for helpful advice on numerical methods, analysis, writing, and life.

My external reviewer, **Yannis Kevrekidis**, for helpful comments and for pointing me to important references.

Some might say knowledge is food for the mind but I tend to believe that *food* is food for the mind. So thanks to:

The CSGF Program for buying the groceries

Mac for the New Mexican green chiles

Ehud (cappuccino) and **Liora** (latte) for the coffee breaks

Dave L. for always thinking of the six-foot sandwiches

Bruce B. for keeping Pizza City in business

Lois for the miracle loaves of bread

Kathleen for sneaking brownies to me before seminars

Bob for the hottest ever chocolate covered habaneros (ooooeee!)

Karla for the coffee beans (huh? Coffee...)

Tom at Pizza City for “The Sleeper” - a slice with green chile

Melanie for the Asian food

Marc C. for the tandoor (I give you free!)

Howard for the mule driver salsa (hiyyah!)

Mark H. for the Smoky Westerns and Newcastle Brown Ale

Dave Ropp for the cookies

John G. for the Scotch whisk(e)y

Anu for the sahmber and idlis

Sarah for whatever that Ethiopian stuff was (yum)

Peter for the chipotle and tomatillo salsa (smoky *and* tangy)

Elizabeth for showing me how to mix sweet and sour

Thor for the panang gai

Mom and Dad for giving me all the recipes

Kj for adding the spice

Well, now I’m hungry again.

Contents

Abstract	ix
1 Introduction	1
1.1 Introduction to Reaction-Diffusion Equations	2
1.2 The Model Equations	4
1.3 Systems With Similar Phenomenology	7
1.3.1 Semiconductor Resonator	7
1.3.2 FIS Reaction	10
1.4 Scope of the Dissertation	12
2 Patterns in One Dimension	15
2.1 Front Solutions	16
2.2 A Front Bifurcation	17
2.2.1 “Domain Walls in Non-Equilibrium Systems and the Emergence of Persistent Patterns”	17
2.3 Ising and Bloch Walls	17
2.4 The NIB Bifurcation for $\epsilon/\delta \ll 1$	18
2.5 Front Transitions	21
2.5.1 Transitions Induced by Convection	23
2.5.2 Oscillating Domains	25
2.5.3 Mechanisms for Front Transitions	25
2.6 “Spatiotemporal Oscillations in a Semiconductor Étalon”	26
3 Patterns in Two Dimensions	30
3.1 Transverse Instability	30
3.2 Labyrinthine Patterns	33
3.3 Single Spot Dynamics	34
3.4 “From Labyrinthine Patterns to Spiral Turbulence”	35
3.5 Spiral Turbulence Revisited	36
3.6 Spiral Breakup by an External Convective Field	37

4 Numerical Methods	49
4.1 Spatial Discretization	49
4.2 Time Integration Methods	51
4.3 Solution of the Nonlinear System	54
5 Conclusion	57
A Domain Walls in Nonequilibrium Systems and the Emergence of Persistent Patterns	64
B Pattern Formation in Dissipative Nonvariational Systems: The Effects of Front Bifurcations	65
C Spatiotemporal Oscillations in a Semiconductor Étalon	66
D From Labyrinthine Patterns to Spiral Turbulence	67
E Scaling of the Semiconductor Equations	68

List of Figures

1.1	Potential function for a scalar reaction-diffusion equation	3
1.2	Nullclines for R-D model: Excitable case	6
1.3	Pulse solution	7
1.4	Nullclines for R-D model: Hopf-Turing case	8
1.5	Turing pattern	9
1.6	Nullclines for R-D model: Bistable case	10
1.7	Front solution	11
1.8	Isoclines for semiconductor model	13
2.1	Right traveling front solution	18
2.2	Stationary front solution	19
2.3	Ising and Bloch angles	19
2.4	The symmetric NIB bifurcation in the (c, η) plane	21
2.5	The nonsymmetric NIB bifurcation in the (c, η) plane	22
2.6	Front velocity vs. perturbation	23
2.7	Front velocity vs. convective perturbation for three cases	24
2.8	Front velocity vs. convective perturbation	25
2.9	Front transition and pulse annihilation	26
2.10	Front velocity vs. convective perturbation - stationary front	27
2.11	Stationary and oscillating fronts	28
2.12	Front velocity vs. convective perturbation - oscillatory front	28
2.13	Front velocity vs. a_0 for three cases	29
3.1	The NIB bifurcation and the transverse instability lines in the $\epsilon - \delta$ parameter plane, symmetric case	32
3.2	The NIB bifurcation and the transverse instability lines in the $\epsilon - \delta$ parameter plane, symmetric case	33
3.3	Front velocity vs. curvature	39
3.4	A map of the velocity vs. curvature relation in the $\epsilon - \delta$ plane	40
3.5	Labyrinthine pattern	41
3.6	Curvature vs. time for a stationary disk	42
3.7	Curvature vs. time for an oscillating disk	42
3.8	Spot splitting	43

3.9	Number of vortices vs. time	44
3.10	Spiral turbulence	45
3.11	Spiral turbulence	46
3.12	Spiral breakup due to convection	47
3.13	Spiral breakup due to convection - closeup	48

List of Tables

1.1	Parameters for semiconductor model	12
1.2	Rate constants for FIS model	14

Abstract

This is a study of fronts and patterns formed in reaction-diffusion systems. A doubly-diffusive version of the two component FitzHugh-Nagumo equations with bistable reaction dynamics is investigated as an abstract model for the study of pattern phenomenologies found in many different physical systems. Front solutions connecting the two stable uniform states are found to be key building blocks for understanding extended patterns such as stationary domains and traveling pulses in one dimension, and labyrinthine structures, splitting spots, and spiral wave turbulence in two dimensions.

The number and type of front solutions is controlled by a bifurcation that we derive both analytically and numerically. At this bifurcation, called the nonequilibrium Ising-Bloch (NIB) bifurcation, a single stationary Ising front loses stability to a pair of counterpropagating Bloch fronts. In two dimensions, we derive a boundary where extended fronts become unstable to transverse perturbations. In addition, near the NIB bifurcation, we discover a multivalued relation between the front speed and general perturbations such as curvature or an external convective field. This multivalued form allows perturbations to induce transitions that reverse the direction of front propagation. When occurring locally along an extended front, these transitions nucleate spiral-vortex pairs.

The NIB bifurcation and transverse instability boundaries divide parameter space into regions of different pattern behaviors. Before the bifurcation, the system may form transient patterns or stationary domains consisting of pairs of Ising fronts. Above the transverse instability boundary, two-dimensional planar fronts destabilize, grow, and finger to form a space-filling labyrinthine, or lamellar, pattern. Beyond the bifurcation the multiplicity of Bloch front solutions allows for the formation of persistent traveling pulses and spiral waves. Near the NIB bifurcation there is an intermediate region where new unexpected patterns are found. One-dimensional stationary domains become unstable to oscillating or breathing domains. In two dimensions, the transverse instability and local front transitions are the mechanisms behind spot splitting and the development of spiral wave turbulence. Similar patterns have been observed recently in the ferrocyanide-iodate-sulfite reaction.



Chapter 1

Introduction

On a recruiting visit to the University of Arizona Program in Applied Math I attended a seminar where Art Winfree mixed a mysterious combination of chemicals in small petri dishes. Minutes later, as the prospective students looked on, beautiful target patterns and spiral waves formed in the dishes. A year later, when I arrived as a new graduate student, I heard Al Scott explain how impulses travel down an giant squid axon as electrical pulses. When I began studying nonlinear optics, Jerry Moloney suggested a problem modeling the light output from a semiconductor placed in a mirrored optical resonator. Although these systems are from chemistry, biology, and optics, they have at least one common feature: the dynamics of the patterns they produce can be modeled by reaction-diffusion equations.

In the fall of 1991, Ehud Meron arrived at the University of Arizona and we soon discovered our common interest in patterns formed by reaction-diffusion systems. He had just finished a review paper on one-dimensional and two-dimensional patterns in excitable media, and I had been doing numerical studies of the semiconductor system. We started analyzing the two-component reaction-diffusion model of the semiconductor resonator. Numerical simulations showed that stationary pulses in the semiconductor system destabilized and started oscillatory motion. Oscillations had been observed in experimental setups of the resonator and we wanted to understand the mechanism behind them.

We realized that to make progress on that system we would first need to understand a simpler model. Studying a simpler model had the advantage that our results might be more generally applicable to other systems of the same class. With this in mind, we set off studying a bistable generalization of the FitzHugh-Nagumo equations. This reaction-diffusion model has the same flavor as the semiconductor system but trades the complicated trigonometric nonlinearity for a simpler cubic form.

In addition to the well known traveling fronts and pulses we found oscillating and stationary domains. In two dimensions we found stationary labyrinthine patterns, spiral waves, spot splitting, and spiral turbulence. We also discovered that an external convective field can cause breakup of a regular rotating spiral pattern.

We took a different approach than most previous authors and studied the reaction-diffusion model from the context of “domain walls”, or front solutions. This approach led us down an inter-

esting path starting with the analysis of a bifurcation that we now call a nonequilibrium Ising-Bloch (NIB) front bifurcation (see Section 2.3 for the definitions of “Ising” and “Bloch” fronts in this context). At a NIB bifurcation, a single stationary front becomes unstable and a pair of counter-propagating fronts appears. Before the bifurcation, combinations of front solutions give rise to stationary and oscillating pulses. The stationary pulses are stable until the NIB bifurcation is approached and then oscillations in the width of the pulse set in. Beyond the bifurcation, multiplicity of fronts leads to the formation of traveling pulses. The key idea is to use the knowledge of the existence and type of different fronts to predict behavior of more complicated solutions consisting of multiple fronts.

In two dimensions we derived a relation to predict when planar fronts become unstable to transverse perturbations. For stationary patterns the transverse instability causes planar fronts to deform and finger into complex labyrinthine, or lamellar, patterns. Near the NIB bifurcation, the transverse instability is one mechanism for causing portions of traveling waves to spontaneously change direction. When directional transitions occur locally on two dimensional fronts, pairs of spiral vortices are nucleated. For appropriate parameters and initial conditions, the system evolves to a state of spiral turbulence characterized by the continuous creation and annihilation of spiral-vortex pairs.

A similar analysis also shows how planar fronts may make spontaneous directional transitions under the influence of general perturbations. These transitions reverse the direction of propagating fronts (or segments of fronts in two dimensions) and induce breakup of regular patterns. This latter discovery led us to unify our ideas for the mechanisms behind spot splitting, spiral turbulence and the breakup due to external convective forcing. For spot splitting we showed that the driving mechanism behind front transitions is curvature of two-dimensional domains. Front transitions in the spiral turbulence regime are induced by either a transverse instability, front interactions, or both. External forcing provides the mechanism for front transitions in the breakup of a regular spiral pattern due to convection.

The combination of the NIB bifurcation, transverse instability, and front transition analysis provide a map to the patterns found in the two-dimensional system: spiral waves, target patterns, labyrinthine patterns, spot replication, and spiral turbulence. This dissertation is a tour of the modeling, theory, analysis, and numerical simulation of those patterns. Sometimes the tour will be mathematical, sometimes physical, sometimes numerical, and sometimes heuristic.

1.1 Introduction to Reaction-Diffusion Equations

Reaction-diffusion systems refer to the class of partial differential equations where the right hand side of a time-dependent equation can be divided into a local (in space) “reaction” part and a nonlocal “diffusion” part. These equations are an abstract model for pattern formation but in many cases have direct application to the fields of developmental biology, chemistry, optics, and branches of applied mathematics. For biological and chemical systems, for example, reaction-diffusion equations represent a reduced description of a complicated set of reactions. The important aspect of all of the applications is that the simple combination of reactions plus transport due to diffusion is sufficient to produce a large variety of interesting patterns.

The general form of reaction-diffusion equations in one dimension is [1]

$$\mathbf{U}_t = \mathbf{f}(\mathbf{U}) + D\mathbf{U}_{xx}, \quad (1.1)$$

where the subscripts denote partial derivatives of the vector \mathbf{U} . The function, $\mathbf{f}(\mathbf{U})$ (likely non-linear!), contains the “reaction” terms and the spatial derivatives denote the “diffusion” terms. The constant matrix D represents the diffusion or transport rate of each species.

The simplest example is the scalar equation [2],

$$u_t = f(u) + u_{xx}. \quad (1.2)$$

Consider an f that has three zeros and varies with a parameter v , such as $f = u - u^3 - v$. The energy, $\mathcal{E} = \int^u f(y) dy = -u^2/2 + u^4/4 + vu$, has a double well form for v values in the range

$$\frac{-2}{3\sqrt{3}} < v < \frac{2}{3\sqrt{3}}, \quad (1.3)$$

as in Fig. 1.1. The two wells correspond to the two stationary homogeneous solutions, $u = u_+(v)$ and $u = u_-(v)$, of

$$u_t = -\delta\mathcal{F}/\delta u = u - u^3 - v + u_{xx}, \quad (1.4)$$

with \mathcal{F} the formal Lyapunov functional

$$\mathcal{F} = \int [\mathcal{E}(u) + u_x^2/2] dx. \quad (1.5)$$

[3, 4]. The functional \mathcal{F} is infinite on unbounded domains but in cases studied in this dissertation we will often consider finite or periodic systems where it is finite.

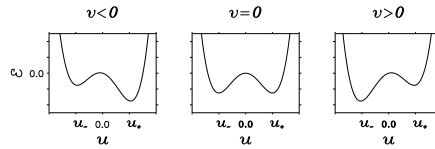


Figure 1.1: The potential function \mathcal{E} for different values of the parameter v .

Front solutions connecting the two homogeneous states of (1.4) satisfy $u_{\chi\chi} + cu_{\chi} + u - u^3 - v$ where $\chi = x - ct$ is the coordinate in the moving frame, and

$$c = \frac{\mathcal{E}(u_-) - \mathcal{E}(u_+)}{\int_{-\infty}^{+\infty} u'(v)^2 d\chi}, \quad (1.6)$$



is the front speed. Since the denominator in (1.6) is always positive, the direction of front propagation is controlled by the relative sizes of $\mathcal{E}(u_-)$ and $\mathcal{E}(u_+)$. Fronts always propagate in the direction that takes the system to the lowest energy, \mathcal{E} . When $v < 0$, $c > 0$ and the front propagates to the right (towards larger x values) and when $v > 0$, $c < 0$ and the front propagates to the left. When $v = 0$ the front is stationary.

1.2 The Model Equations

Early studies of fronts in reaction-diffusion models began with Luther's work around the turn of the century [5, 6]. Later, Fisher [7] and Kolmogorov *et al.* produced theoretical treatments. Even more studies were inspired by Turing's famous paper [8] showing how uniform systems may be unstable to finite wavenumber perturbations. More researchers picked up the theme and studies of reaction-diffusion models have reached into many disciplines. See the review articles [2, 9, 10, 11] for summaries of earlier works.

One of the most famous reaction-diffusion models is the Fitzhugh-Nagumo model for the conduction of electrical impulses along a nerve fiber [12, 13, 14]. The original heuristic model for the flow of electric current through the surface membrane of a giant squid axon was proposed by Hodgkin and Huxley in 1952 [15]. The proposed four component model represents equations for the membrane current density, the sodium activation, the sodium inactivation, and the potassium activation in the nerve axon. FitzHugh simplified these equations by proposing the following pair of equations he called the Bonhoeffer-van der Pol (BVP) model

$$\begin{aligned} J &= \frac{1}{c}u_t - u + u^3 - v, \\ cv_t + bv &= a - u, \end{aligned} \tag{1.7}$$

where J is the current density, u represents the combined membrane voltage and sodium activation, and v represents the combined sodium inactivation and potassium activation. The parameters a , b , and c are constants (see [12, 13] for details). Using an analog computer and phase plane projections, FitzHugh showed that the dynamics of this model were qualitatively the same as the dynamics of the more complicated four variable Hodgkin-Huxley model.

Nagumo *et al.* studied the same equations but simulated them in an electric circuit [13] as a distributed line. The equations they used show explicitly the diffusion

$$\begin{aligned} hu_{ss} &= \frac{1}{c}u_t - u + u^3 - v, \\ cv_t + bv &= a - u, \end{aligned} \tag{1.8}$$

with the constant h related to the density of the resistance per unit length in the line. Both FitzHugh and Nagumo found that this model allows for the propagation of pulses and pulse trains, where the pulses represent an excited domain or electrical signal.

The reaction diffusion model studied in this dissertation is a direct extension of Eqns. (1.8). First let $x = \sqrt{h} s$, and replace t with t/c , and v with $-v$. Then, setting $\epsilon = 1/c^2$, the equations



take the form

$$\begin{aligned} u_t &= u - u^3 - v + u_{xx}, \\ v_t &= \epsilon(u - bv + a). \end{aligned} \tag{1.9}$$

Next, identify the parameters $a_1 = b$, $a_0 = -a$, and add a diffusion term with coefficient δ to the second (v) equation. Extended into two dimensions the resulting model equations are

$$\begin{aligned} u_t &= u - u^3 - v + \nabla^2 u, \\ v_t &= \epsilon(u - a_1 v - a_0) + \delta \nabla^2 v. \end{aligned} \tag{1.10}$$

The four parameters $a_1, a_0 \in \mathcal{R}$, $\epsilon > 0$, and $\delta > 0$ are adjustable in the model and control the number and type of fixed points. The parameters a_1 and a_0 determine the reaction kinetics; *i.e.* how many homogeneous stationary states are available. The time-scale ratio between the two fields, ϵ , and diffusion coefficient ratio, δ , determine the stability of those solutions and also will serve as bifurcation parameters in the analysis of Chapter 2. In some cases we will study the one-dimensional version of (1.10) where u and v are functions of x and t only.

Typically Eqns. (1.10) are scaled with $1/\epsilon$ in front of the u reaction terms. There is a practical advantage when doing numerical simulations for scaling with the ϵ in front of the v reaction terms. In this case, the narrow u front is always of size $\mathcal{O}(1)$ and when ϵ is decreased the pattern size gets larger instead of the front size getting smaller. It is obvious then, when varying parameters (say making ϵ smaller) that the domain size must be increased to fit the pattern solution and correspondingly the number of computational points must be increased. This scaling makes it simpler to keep a constant number of grid points across a front region when varying system parameters.

In the context of chemical reactions, the field u is interpreted as the activator and v the inhibitor; the growth of u stimulates growth of both u (as long as $|u| < 1$) and v while the growth of v causes decay in both u and v . In certain contexts u is referred the autocatalyst and v the reactant. Most studies of activator-inhibitor systems consider $\epsilon \ll 1$ where u is the fast variable and v is the slow variable. The study presented in this dissertation encompasses all positive values of ϵ , both small and large.

The stationary homogeneous solutions of (1.10) are found by setting the derivatives equal to zero and looking for intersections of the nullclines

$$\begin{aligned} u - u^3 - v &= 0, \\ u - a_1 v - a_0 &= 0. \end{aligned} \tag{1.11}$$

In Figs. 1.2, 1.4, 1.6, we have identified the three basic cases for intersections of the nullclines. In Fig. 1.2 the nullclines intersect at a single point on an outer branch of the cubic nullcline; in Fig. 1.4 at a single point on the middle branch of the cubic nullcline; and in Fig. 1.6 there are three intersections, two on the outer branches and one on the middle branch.

When the nullclines intersect at a single point lying on an outer branch of the cubic nullcline (Figure 1.2) and ϵ is small, the dynamics are “excitable” and describe the situation in an active medium such as a nerve fiber. The single fixed point is stable but perturbations past the excitation

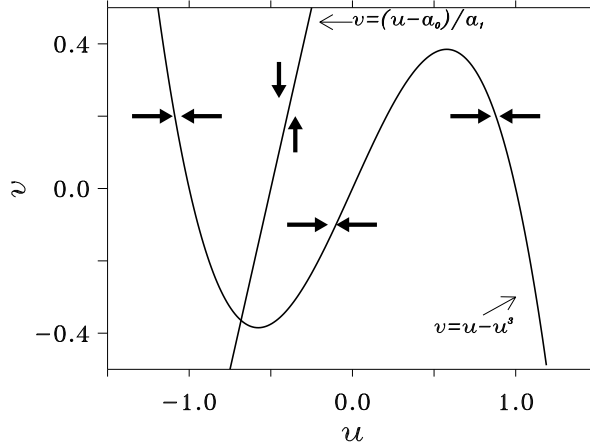


Figure 1.2: The nullclines of Equation (1.10) for the case of an excitable system. The arrows indicate the direction of the flow.

threshold cause a large excursion in phase space before returning to the fixed point. Since there is only one uniform state, isolated front solutions are not possible. It is possible, however to have both traveling and stationary pulses of excited regions. A typical solution profile with the corresponding phase plane picture are shown in Figure 1.3.

When the nullclines intersect at a single point on the middle branch of the cubic nullcline (Figure 1.4) the uniform solution may lose stability in two different ways, either to a spatial pattern or to temporal oscillations. For illustration, let $a_0 = 0$ and $a_1 < 1$. Then the state $(u, v) = (0, 0)$ is the single homogeneous solution. This homogeneous state loses stability to a spatial pattern through a Turing bifurcation [8] at

$$\mu = \mu_c = 2 - a_1 + 2\sqrt{1 - a_1} \quad \text{with} \quad \epsilon > \frac{1}{a_1}, \quad (1.12)$$

where $\mu = \delta/\epsilon$. For $\mu > \mu_c$ the system forms a stationary periodic pattern at a finite wavenumber given by

$$k_c = \left(\frac{1 - a_1 + \sqrt{1 - a_1}}{2 - a_1 + 2\sqrt{1 - a_1}} \right)^{1/2}. \quad (1.13)$$

When $\epsilon \ll \epsilon_{HB} = 1/a_1$, the solution $(u, v) = (0, 0)$ loses stability through a Hopf bifurcation and uniform oscillations set in. A typical solution profile for a one-dimensional pattern formed through the Turing instability is shown in Figure 1.5.

Finally, when the nullclines intersect at three points each on a different branch of the cubic nullcline (Figure 1.6) the system is bistable. Each of the two fixed points on the outer branches represent stable uniform solutions while the fixed point on the inner branch is unstable to uniform

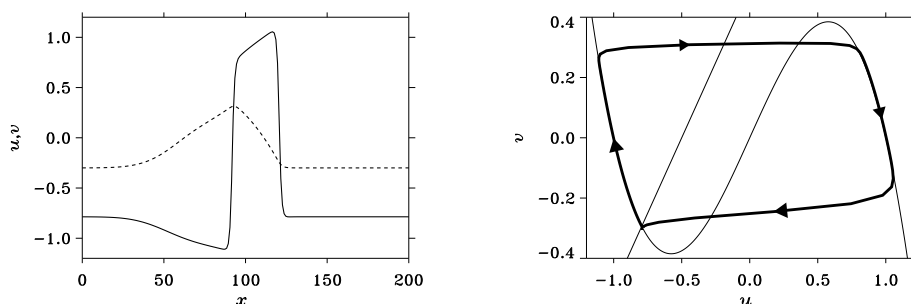


Figure 1.3: An excitable system: typical pulse solution and corresponding diagram in the (u, v) phase plane. The solid line is the u field and the dashed line is the v field. Parameters: $\epsilon = 0.01$, $\delta = 1.0$, $a_1 = 1.0$, $a_0 = -0.5$.

perturbations. In addition to the two stable solutions now there may also be front solutions connecting the two uniform stable states. A typical front solution profile is shown in Figure 1.7 with its corresponding phase plane diagram.

1.3 Systems With Similar Phenomenology

This section describes two reaction-diffusion systems that have characteristics similar to the model considered in this dissertation. The first, a semiconductor resonator, share a similarity in the form of the equations; the model has two fields and the dynamics are excitable, bistable, or oscillatory depending on parameters. It also has the extra twist that one of the system parameters varies nonuniformly in space.

In parallel with our analysis and numerical modeling, new chemical experiments exhibiting similar spatiotemporal patterns were being performed. A group at the Center for Nonlinear Dynamics at the University of Texas published patterns formed by the ferrocyanide-iodate-sulfite (FIS) reaction that display spiral turbulence, labyrinthine patterns, and spot-replication. This reaction shares many similar patterns as solutions to Eqns. (1.10) and the semiconductor system although the models of the FIS reaction have significantly different reaction kinetics.

1.3.1 Semiconductor Resonator

One application of reaction-diffusion equations outside the context of either biology or chemistry is a model for a semiconductor medium placed between two partially reflective mirrors. In this configuration, known as a semiconductor Fabry-Perot resonator (or étalon), the input parameter is an incident light beam and the multivalued or oscillatory output is the transmitted light intensity from the cavity. Optical bistability in a semiconductor was demonstrated experimentally in 1978 by McCall [16] and oscillations were observed in 1992 by Grigor'yants and Dyuzhikov [17].

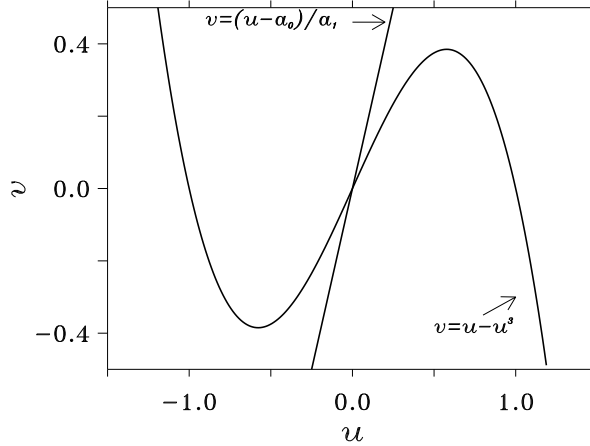


Figure 1.4: The nullclines of Equation (1.10) for the case of a Hopf-Turing type system.

When an input beam shines on the material some of the light is reflected back and some enters the cavity where it may resonate at frequency modes dependent on both the size of the cavity and the intensity of the input beam. The semiconductor refractive index is nonlinearly dependent on the intensity of the light in the cavity. Changing the intensity of the light can effectively tune the cavity in and out of resonance. Coupled to the feedback from the mirrors, this nonlinear dependence gives rise to a hysteresis in the transmitted intensity allowing for more than one possible output value for a single input beam intensity.

The proposed model for this system is a pair of coupled reaction-diffusion equations for the carrier density, N , and temperature, T in the semiconductor [18, 19]

$$\begin{aligned} N_t &= \frac{\alpha I(N, T)}{\hbar\omega} - \frac{N}{\tau_N} + D\nabla^2 N, \\ T_t &= \frac{qN}{C\rho\tau_N} - \frac{(T - T_0)}{\tau_T} + \kappa\nabla^2 N. \end{aligned} \quad (1.14)$$

The number of carriers, N , increases by absorption of an optical photon proportional to the light intensity I with α the absorption coefficient. The carriers decrease by recombination with holes with a characteristic time scale τ_N , and diffuse transversely with diffusion coefficient D . The temperature, T , increases by recombinative heating with q the heat of one recombination event, C and ρ the specific heat and density of the semiconductor. The temperature decreases with heat sinking to the ambient temperature T_0 on a characteristic time τ_t and diffuses transversely with diffusion coefficient κ . Typical parameter values are given in Table 1.1.

In general we would have to solve the transverse field equation for the electric field in the cavity [20]. If we restrict ourselves to small cavities where the round-trip time for the light is much

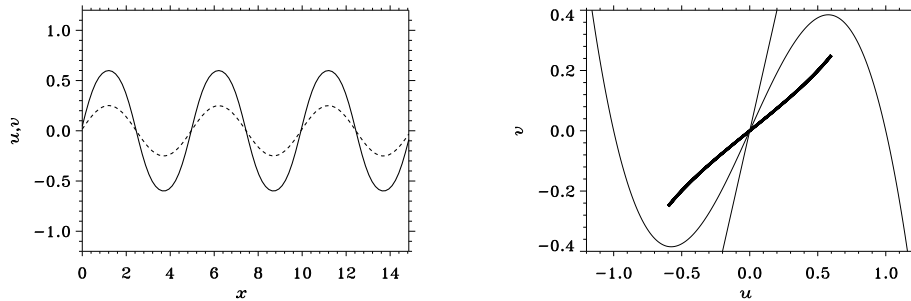


Figure 1.5: A Hopf-Turing system: A typical pulse solution in and corresponding diagram in the (u, v) phase plane for a pattern formed beyond the Turing instability. The solid line is the u field and the dashed line is the v field. The phase plane shows that for small wavelength patterns the trajectory does not reach the cubic nullcline. Parameters: $\epsilon = 1.00$, $\delta = 0.01$, $a_1 = 0.5$, $a_0 = 0.0$.

shorter than the electron-hole recombination time and assume that longitudinal density variations are small the model simplifies; we can ignore self-focusing and diffraction of the light in the semiconductor. Using the boundary conditions for the Fabry-Perot cavity [21], the light intensity averaged over the thickness of the cavity is given by

$$I(N, T) = \frac{I_0(1 - R)(1 - e^{-\alpha l})(1 + Re^{-\alpha l})}{(1 - 2Re^{-\alpha l} \cos(4\pi nl/\lambda) + R^2e^{-2\alpha l})\alpha l}, \quad (1.15)$$

where l is the length of the cavity, λ the wavelength of the input beam and R is the reflectivity of the mirrors. Generation of carriers and heating both change the refractive index of the material each with different sign,

$$n(N, T) = n_0 - \sigma N + \gamma T, \quad (1.16)$$

where σ and γ are positive constants and n_0 is the initial refractive index.

The typical recombination time τ_N is much shorter than the characteristic cooling time τ_T , so the dynamics of the carriers takes place on a much faster time scale than the temperature fluctuations. This disparity of time scales creates a stiff pair of equations.

The model equations can be scaled to dimensionless form to aid in analysis and simulation (Appendix E). A suitable scaling leaves the following two-component system,

$$\begin{aligned} u_t &= I_0 W(u, v) - u + \nabla^2 u, \\ v_t &= \epsilon(u - v/\bar{\tau}) + \delta \nabla^2 v, \end{aligned} \quad (1.17)$$

$$W(u, v) = \frac{(1 - R)(1 - e^{-\alpha l})(1 + Re^{-\alpha l})}{(1 - 2Re^{-\alpha l} \cos(n(u, v)) + R^2e^{-2\alpha l})}, \quad (1.18)$$

$$n(u, v) = \beta - \beta_N u + \beta_T v, \quad (1.19)$$

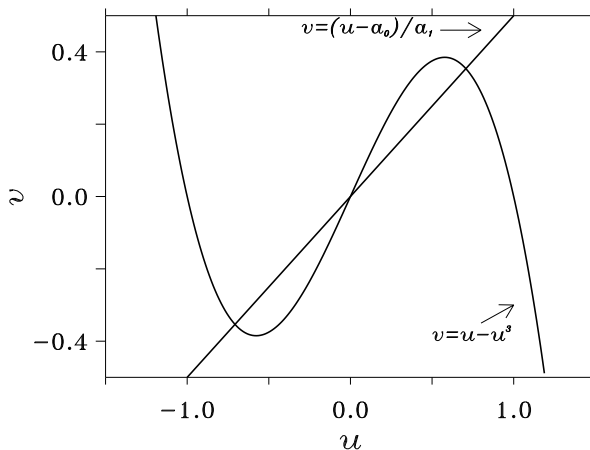


Figure 1.6: The nullclines of Equation (1.10) for the case of a bistable system.

where the sizes of the variables u and v are of $O(1)$ and ϵ is a small parameter. Scalings that convert the dimensionless parameters to physical quantities are in Appendix E.

Figure 1.8 shows isoclines for Eqs. (1.17). Notice that they take nearly the same form as for the model reaction-diffusion equations studied in this dissertation (compare with Fig. 1.6), with the exception that the trigonometric nonlinearity allows for the possibility of more than three fixed points. For example, the system can have three stable fixed points or have one stable fixed point and one oscillatory point. For that reason this system can have a dazzling variety of complex temporal and spatiotemporal dynamics [17].

1.3.2 FIS Reaction

Recent experiments in a gel-filled chemical reactor have been performed on the ferrocyanide-iodate-sulfite (FIS) reaction [22, 23, 24]. Many different spatial patterns were observed: stationary labyrinthine patterns (lamellae), splitting spots, repulsive front interactions, and traveling waves that collide and annihilate. This was the first time labyrinthine patterns and spot splitting were observed in a chemical system. It was also the first observation in a chemical system of approaching fronts that slow and stop at a finite separation. All of these behaviors are manifested in the reaction-diffusion model studied in this dissertation.

Several models for the kinetics of this reaction have been proposed. Edlbom *et al.* proposed a model with twelve reacting species [25], and Gáspár and Showalter developed a similar ten-species model [26, 27]. As a further simplification they derived a reduced model of four species, SO_3^{2-} ,



CHAPTER 1. INTRODUCTION

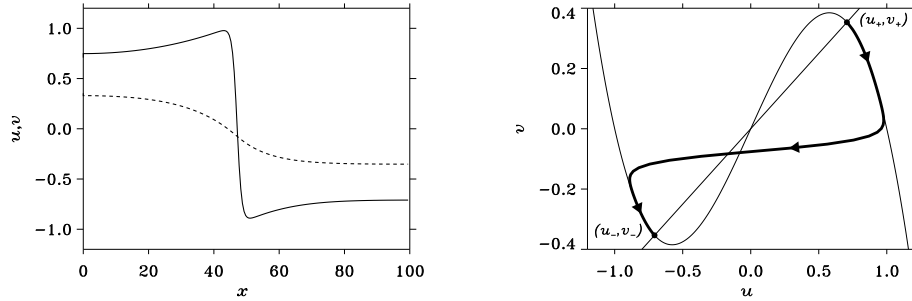


Figure 1.7: A bistable system: A typical front solution in and corresponding diagram in the (u, v) phase plane. The solid line is the u field and the dashed line is the v field. Parameters: $\epsilon = 0.01$, $\delta = 2.0$, $a_1 = 2.0$, $a_0 = 0.0$.

$H\text{SO}_3^-$, H^+ , and I_2 (see [24] for details). The model reads

$$\begin{aligned}
 X_t &= k_1 AY - (k_{-1} + k_2 + k_0)X - k_4 ZX + D_x X_{xx}, \\
 Y_t &= -k_1 AY + (k_{-1} + k_2)X - 2k_3 Y^2 + 3k_4 ZX + k_0(Y_0 - Y) + D_y Y_{xx}, \\
 Z_t &= k_3 Y^2 - k_4 ZX - (k_5 + k_0)Z + D_Z Z_{xx}, \\
 A_t &= -k_1 AY + k_{-1}X + k_0(A_0 - A) + D_A A_{xx}.
 \end{aligned} \tag{1.20}$$

Typical parameters are [24] $D_Y = D_Z = D_A = 1.0 \times 10^{-5} \text{cm}^2/\text{s}$, $D_x = 2.0 \times 10^{-5} \text{cm}^2/\text{s}$, with the reaction rates, k_i 's, summarized in Table 1.2. For typical parameter values $[Fe(CN)_6^{-4}]_0 = 2.0 \text{mM}$, $[IO_3^-]_0 = 75.0 \text{mM}$, $[SO_3^{2-}]_0 = 89.3 \text{mM}$, and $k_0 = 0.014 \text{s}^{-1}$ the dynamics are very “stiff”: the time scales of the reactants vary widely. For example, k_1 and k_2 differ by about ten orders of magnitude. While this can be a disadvantage when doing numerical simulations as discovered by Lee and Swinney [24], it may be possible to take advantage of the disparate time scales and reduce the model further by eliminating the fast reacting species. Appropriate reductions may produce a new system with cubic nonlinearities [24].

Because of the difficulty of computing the FIS reaction in large systems a similar two species model, the Gray-Scott model [28, 29, 30], has often been used instead [31, 32]. Neither that model nor the proposed model for the FIS reaction (even in its simplified four species version!) is of the same form as the reaction-diffusion model considered in this dissertation. Amazingly, regardless of the exact details of the chemical kinetics, many of the pattern behaviors found in the FIS models and the model considered here are similar.



Table 1.1: Parameters for semiconductor model

Characteristic recombination time (carrier lifetime)	τ_N	3.1×10^{-7}
Characteristic thermal time	τ_T	0.01s
Wavelength	λ	$5.6 \mu m$
Heat produced by single recombination	q	$\hbar\omega J$
Specific heat density	C	$9.6 \times 10^{-2} \text{ J/gK}$
Semiconductor density	ρ	5.8 g/cm^3
Ambient temperature	T_0	77 K
Carrier generation contribution to refractive index	σ	4.1×10^{-3}
Thermal contribution to refractive index	γ	6.1×10^{-4}
Initial refractive index	n_0	0
Absorption coefficient	α	6 cm^{-1}
Band edge thermal coefficient	θ	17.5
Mirror reflectivity	R	0.36
Semiconductor thickness	l	0.02 cm

1.4 Scope of the Dissertation

The theory and application of reaction-diffusion models reaches far and wide. In this dissertation I can only scratch the surface and make a few stabs into the unknown. Since a portion of these results have already been published I have chosen to include those results as reprints in the appendices to this dissertation. The layout reflects the structure for this type of dissertation as dictated by the University of Arizona Graduate College requirements.

Chapter 1 - Introduction Introduction to reaction-diffusion systems, the model reaction-diffusion equations, and a description of a few similar models

Chapter 2 - Patterns in one-dimension A study of front, pulse, stationary and oscillating solutions to the reaction-diffusion model equations

Chapter 3 - Patterns in two-dimensions Analysis and computation of labyrinthine patterns, spiral waves, spot replication, and spiral turbulence

Chapter 4 - Numerical methods Description of numerical techniques

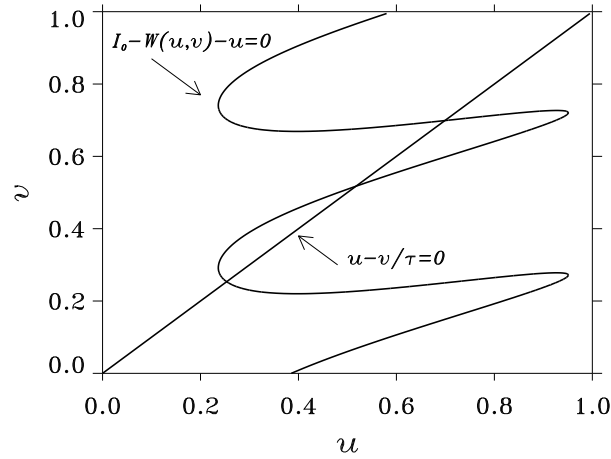


Figure 1.8: Isoclines for the scaled semiconductor model of Eqns (1.17). The lower fixed point is stable (excitable), the middle one is unstable and the top is of Hopf-Turing type. Parameters: $\tau = 1$, $I_O = 8.0$, $R = 0.36$, $\alpha = 3.2$, $l = 0.02$, $\beta = 0.0$, $\beta_N = 4.0$, $\beta_T = 14.0$.

Chapter 5 - Conclusion Summary and conclusion

Appendix A - Paper A “Domain walls in nonequilibrium systems and the emergence of persistent patterns”

Appendix B - Paper B “Pattern formation in dissipative nonvariational systems: the effects of front bifurcations”

Appendix C - Paper C “From labyrinthine patterns to spiral turbulence”

Appendix D - Paper D “Spatiotemporal oscillations in a semiconductor étalon”



Table 1.2: Rate constants for FIS model

k_1	$5.0 \times 10^{10} M^{-1} s^{-1}$
k_{-1}	$8.1 \times 10^3 s^{-1}$
k_2	$8.0 \times 10^{-1} \times [IO_3^-]_0 M^{-1} s^{-1}$
k_3	$1.0 \times 10^6 \times [IO_3^-]_0 M^{-2} s^{-1}$
k_4	$2.3 \times 10^9 M^{-1} s^{-1}$
k_5	$1.2 \times 10^3 \times [Fe(CN)_6^{4-}]_0 M^{-1} s^{-1}$



Chapter 2

Patterns in One Dimension

Although many real world patterns are two or three dimensional much insight can be gained by first studying the one dimensional version of Eq. (1.10)

$$\begin{aligned}u_t &= u - u^3 - v + u_{xx}, \\v_t &= \epsilon(u - a_1 v - a_0) + \delta v_{xx}.\end{aligned}\tag{2.1}$$

As described in Chapter 1, the system can be either of excitable, Hopf-Turing, or bistable type depending on the choice of the parameters a_1 and a_0 . In this chapter we will primarily consider the case where a_1 and a_0 are chosen such that the system is bistable as in Fig. 1.6: there are three homogeneous fixed points, two stable ones on the outer branches of the cubic nullcline and one unstable one on the center branch.

Most studies of Eqs. (2.1) have focused on the regime of small ϵ and used that parameter as a basis for a singular perturbation analysis of front and pulse solutions [9, 10, 33]. If the range of ϵ is extended to take on all positive values we find there is a critical value ϵ_c where a front bifurcation occurs; a single stationary front bifurcates to a pair of counterpropagating fronts. This bifurcation, which we call a nonequilibrium Ising-Bloch (NIB) bifurcation, plays a key role determining the types of patterns formed in the system.

For $\delta = 0$ and $a_0 = 0$ the front bifurcation can be found by expanding the stationary front solution in terms of the propagation speed c . When δ is small the result can be extended in powers of δ giving a relation for the front bifurcation line in the $\epsilon - \delta$ parameter plane. For large δ we use a different small parameter, ϵ/δ , in a singular perturbation analysis to find the front bifurcation. For moderate values of δ both approaches break down and the exact front bifurcation is computed numerically.

This chapter focuses on the NIB front bifurcation and the implications it has on pattern formation in one dimension. First we derive front solutions for the model equations (1.10) and explain how front multiplicity may lead to persistent patterns. Next, we analyze the NIB bifurcation when $\delta = 0$ and for the extension to small δ . Since many of the interesting patterns in this model are found for $\delta \neq 0$ we derive the NIB bifurcation in the $\epsilon - \delta$ plane for $\epsilon/\delta \ll 1$. The majority of the one-dimensional analysis and pattern dynamics found in this system are described in A and B.

Summaries of the key results are presented in Sections 2.2.1 and B. In Section 2.3 we explain the terminology of Ising and Bloch fronts in the context of reaction-diffusion systems. Section 2.4 contains a detailed derivation of the front bifurcation when $\epsilon/\delta \ll 1$. An important new result of this chapter is presented in Section 2.5, where we show how the effects of general perturbations, such as an external convective field or front interactions, may induce front transitions. These transitions provide a mechanism for one-dimensional breathing pulses shown in Section 2.5.2. Breathing domains and front transitions will reappear again in the study of two-dimensional spot replication and spiral wave breakup.

2.1 Front Solutions

Front solutions to Eqns. (1.10) play a key role in determining what types of patterns may develop in the system. In the bistable case there are three intersections of the nullclines (1.11). The intersections on the outer branches of the cubic curve are stable uniform solutions, $(u, v) = (u_+, v_+)$ representing the “up” state domain, and $(u, v) = (u_-, v_-)$ the “down” state domain. Front solutions connect regions of up states to down states. There are also fronts that connect either the up state or the down state to the solution $(u, v) = (0, 0)$. Those will not be considered because the solution $(0, 0)$ is always unstable to uniform perturbations in the bistable case. As we will see, the type (stationary or propagating) and stability of these front solutions depends on the sizes of ϵ and δ .

For simplicity consider first a nondiffusing v field, $\delta = 0$. For large ϵ the dynamics of the v field are on a much faster time scale than the u field. If we let $\nu = 1/\epsilon$ and rescale Eq. (2.1) by $\tau = t/\nu$ we find

$$\begin{aligned} u_\tau &= \nu(u - u^3 - v + u_{xx}), \\ v_\tau &= (u - a_1v - a_0). \end{aligned} \quad (2.2)$$

Setting $\nu = 0$, the leading order solution of u is independent of τ and the v Eq. (2.2) can be solved,

$$v(x, t) = v_0(x)e^{-\epsilon a_1 t} + \frac{(u(x, t) - a_0)(1 - e^{-\epsilon a_1 t})}{a_1}. \quad (2.3)$$

After an initial transient the v field is slaved to the u field along the nullcline as $v = (u - a_0)/a_1$. Substituting this into the u equation we have the asymptotic system,

$$u_t = 1 - \frac{1}{a_1}u - u^3 - \frac{a_0}{a_1} + u_{\chi\chi}. \quad (2.4)$$

In the traveling frame, $\chi = x - ct$, constant speed front solutions of Eq. (2.4) satisfy

$$u_{\chi\chi} + cu_\chi + 1 - \frac{1}{a_1}u - u^3 - \frac{a_0}{a_1}, \quad (2.5)$$

with $(u, v) \rightarrow (u_\pm, v_\pm)$ as $\chi \rightarrow \mp\infty$. Since this equation is invariant under the transformation

$$\chi \rightarrow -\chi, \quad c \rightarrow -c, \quad (2.6)$$

symmetric front solutions with $(u, v) \rightarrow (u_\pm, v_\pm)$ as $\chi \rightarrow \pm\infty$ follow directly.

This asymptotic system is gradient, *i.e.* derivable from a potential, and front solutions have speed c as given in the relation for the scalar diffusion equation (1.6). For $a_0 = 0$, the states (u_{\pm}, v_{\pm}) are symmetric, $(u_+, v_+) = -(u_-, v_-)$, and the two potential wells are of equal depth. From (1.6) this implies that the speed of the front is zero. When $a_0 < 0$ fronts propagate to the right and when $a_0 > 0$ they propagate to the left. The exact form of the stationary front solution is

$$\begin{aligned} u_0(\chi) &= -u_+ \tanh(u_+ \chi / \sqrt{2}), \\ v_0(\chi) &= u_0(\chi) / a_1, \end{aligned} \tag{2.7}$$

where $u_{\pm} = \pm \sqrt{1 - a_1^{-1}}$.

For small ϵ the front solutions are different. Since the stationary solution (2.7) does not depend on ϵ it still exists but is now unstable. In addition there are two counterpropagating fronts with their symmetric counterparts; they connect the same asymptotic states at $+\infty$ and $-\infty$ but propagate in opposite directions. As pointed out earlier, the regime of small ϵ and propagating fronts and pulses has been studied extensively [9]. Asymptotic solutions for small ϵ fronts can be derived but in this chapter we will need only the leading order forms near the NIB bifurcation. The key point is that in the range of intermediate ϵ there is a bifurcation from single to multiple solutions. In the next section we will show how to derive this bifurcation point and with it the leading order traveling wave solutions of (2.1).

2.2 A Front Bifurcation

2.2.1 “Domain Walls in Non-Equilibrium Systems and the Emergence of Persistent Patterns”

The analyses and results of this section are described in “Domain walls in non-equilibrium systems and the emergence of persistent patterns.” A. The following is a summary of the main results.

2.3 Ising and Bloch Walls

The internal structure of the traveling front solutions differs from that of the stationary front. For traveling fronts, the leading order v field is translated with respect to the u field by the amount ca_1 . Since the parameter a_1 is always positive, for traveling fronts the v field always lags behind the u field as in Figure 2.1. For stationary, $c = 0$, fronts the u and v field both are zero simultaneously as shown in Figure 2.2.

If we introduce the phase $\phi = \arctan(v/u)$, we see that the stationary solution has a constant phase across the front except at the core ($u = 0, v = 0$) where it undergoes a jump of π . The traveling fronts however have a smoothly varying phase and both fields are never simultaneously zero. Figure 2.3 shows the phase ϕ for the front solutions of Figures 2.1 and 2.2.

We refer to the stationary front as an Ising front and the pair of counterpropagating fronts beyond the NIB bifurcation as Bloch fronts. Ising and Bloch fronts in this context were first introduced by Coulet *et al.* [34] as nonequilibrium analogs of Ising and Bloch walls in ferromagnets. In

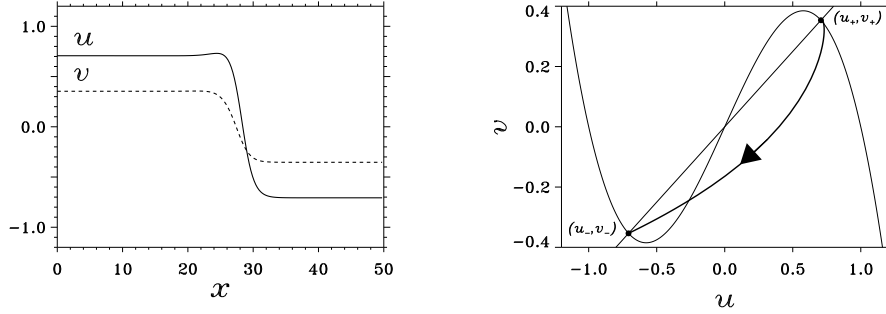


Figure 2.1: (a) Rightward traveling front solution. For traveling fronts the v field always lags behind the u field. (b) Traveling front in the (u, v) phase plane. The arrow indicates the trajectory direction for increasing x .

ferromagnets the angle ϕ would correspond to the angle the magnetization vector makes with the easy magnetization direction [35].

We often refer to the parameter regime (in the $\epsilon - \delta$ plane) where there is only the Ising front as the “Ising regime” and where there are counterpropagating Bloch fronts as the “Bloch regime.”

2.4 The NIB Bifurcation for $\epsilon/\delta \ll 1$

To study the NIB bifurcation in the regime $\epsilon/\delta \ll 1$ we consider one-dimensional front solutions propagating at constant speeds and connecting the up state at $-\infty$ to the down state at $+\infty$. First we rescale time and space according to

$$z = \sqrt{\mu}x, \quad \tau = \epsilon t, \quad \mu = \epsilon/\delta \ll 1, \quad (2.8)$$

and go into the traveling frame, $\zeta = z - c\tau$. The model equations 2.1 then take the form

$$\begin{aligned} \mu u_{\zeta\zeta} + c\delta\mu u_{\zeta} + u - u^3 - v &= 0, \\ v_{\zeta\zeta} + cv_{\zeta} + u - a_1v - a_0 &= 0. \end{aligned} \quad (2.9)$$

Constant speed front solutions of (2.9) can be separated into two parts pertaining to distinct regions: outer regions away from the front, where both u and v vary on a scale of $\mathcal{O}(1)$, and an inner region including the front, where u varies much faster than v . In the outer regions the derivative terms in the u equation of (2.9) can be neglected leading to the solutions $u = u_{\pm}(v)$ of the remaining cubic relation $u - u^3 - v = 0$. Using these forms in the v equation of (2.9), and setting the front position, $u = 0$, at the origin, $\zeta = 0$, we obtain closed equations for v ,

$$v_{\zeta\zeta} + cv_{\zeta} + u_{\pm}(v) - a_1v - a_0 = 0, \quad (2.10)$$

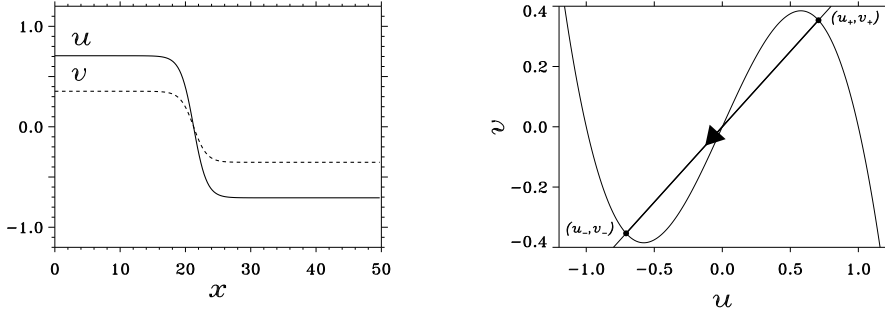


Figure 2.2: (a) Stationary front solution. The u field and v field both go through $(0, 0)$ simultaneously. (b) Stationary front in the (u, v) phase plane. The arrow indicates the trajectory direction for increasing x .

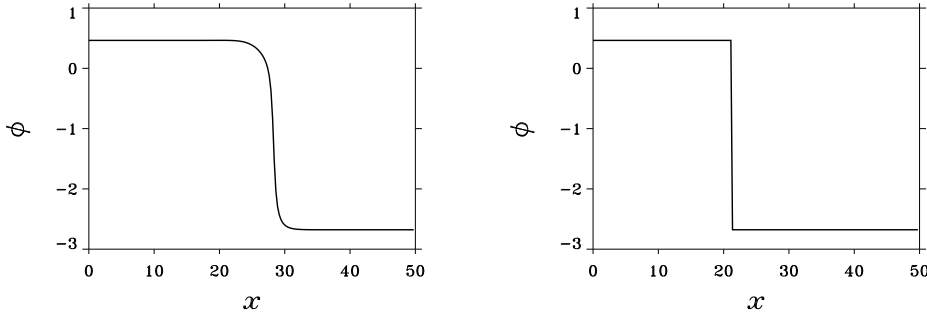


Figure 2.3: The phase angle $\phi = \arctan(v/u)$ for (a) a Bloch front and (b) an Ising front. The Bloch front phase rotates smoothly through π but the Ising front suffers a jump.

with $u = u_+(v)$ when $\zeta < 0$ and $u = u_-(v)$ when $\zeta > 0$. To simplify, we choose a_1 large enough so that $|v| \ll 1$ and the branches $u_{\pm}(v)$ can be approximated by the linear forms $u_{\pm}(v) = \pm 1 - v/2$. We then obtain the following linear boundary value problems for the two outer regions:

$$\begin{aligned}
 \zeta < 0: \quad & v_{\zeta\zeta} + cv_{\zeta} - q^2v + q^2v_+ = 0, & v(0) &= v_f, \\
 & & v(-\infty) &= v_+, \\
 \zeta > 0: \quad & v_{\zeta\zeta} + cv_{\zeta} - q^2v + q^2v_- = 0, & v(0) &= v_f, \\
 & & v(\infty) &= v_-,
 \end{aligned} \tag{2.11}$$

where

$$v_{\pm} = \frac{\pm 1 - a_0}{a_1 + 1/2}, \quad q^2 = a_1 + 1/2, \tag{2.12}$$



CHAPTER 2. PATTERNS IN ONE DIMENSION

and v_f is the value of v at the front position. The solutions are

$$\begin{aligned} v(\zeta) &= (v_f - v_+)e^{\sigma_1\zeta} + v_+, & \zeta < 0, \\ v(\zeta) &= (v_f - v_-)e^{\sigma_2\zeta} + v_-, & \zeta > 0, \end{aligned} \quad (2.13)$$

with

$$\sigma_{1,2} = -c/2 \pm (c^2/4 + q^2)^{1/2}. \quad (2.14)$$

By construction, the two outer solutions for v are continuous at $\zeta = 0$. Matching the derivatives of v at $\zeta = 0$ gives a relation between c , the speed of the front, and v_f , the value of the v field at the front position,

$$v_f = -\frac{c}{2q^2(c^2/4 + q^2)^{1/2}} - \frac{a_0}{q^2}. \quad (2.15)$$

A second relation between v_f and c is obtained by solving the inner problem. In the front region u varies on a scale of $\mathcal{O}(\sqrt{\mu})$ but variations of v are still on a scale of $\mathcal{O}(1)$. Stretching the traveling-frame coordinate according to $\chi = \zeta/\sqrt{\mu}$, we obtain from (2.9)

$$\begin{aligned} u_{\chi\chi} + \eta c u_\chi + u - u^3 - v &= 0, \\ v_{\chi\chi} + \sqrt{\mu} c v_\chi + \mu(u - a_1 v - a_0) &= 0, \end{aligned} \quad (2.16)$$

where $\eta^2 = \epsilon\delta$. Setting $\mu = 0$ in the v equation of (2.16) leaves the equation $v_{\chi\chi} = 0$, and we choose the solution $v = \text{constant}$. Fixing the constant, $v = v_f$, in the equation for u produces a nonlinear eigenvalue problem for c ,

$$\begin{aligned} u_{\chi\chi} + \eta c u_\chi + f(u, v_f) &= 0, \\ u(\mp\infty) &= u_\pm(v_f), \end{aligned} \quad (2.17)$$

with $f(u, v_f) = u - u^3 - v_f$. The cubic function, f , can be rewritten as

$$f(u, v_f) = -[u - u_-(v_f)][u - u_0(v_f)][u - u_+(v_f)], \quad (2.18)$$

where $u_-(v_f) = -1 - v_f/2$, $u_0 = v_f$, and $u_+(v_f) = 1 - v_f/2$, are the linearized forms of the cubic isocline near the three solutions $u = -1, 0, 1$ respectively. The speed of the front solution of (2.17) is

$$\eta c = \frac{1}{\sqrt{2}}(u_+ - 2u_0 + u_-) = \frac{-3}{\sqrt{2}}v_f. \quad (2.19)$$

Combining the two equations (2.15) and (2.19) we find an implicit relation for the front speed, c , in terms of the equation parameters η , a_1 , and a_0 ,

$$\frac{\sqrt{2}}{3}\eta c = \frac{c}{2q^2\sqrt{c^2/4 + q^2}} + \frac{a_0}{q^2}. \quad (2.20)$$



CHAPTER 2. PATTERNS IN ONE DIMENSION

This equation was derived using the coordinate scaling (2.8). The relation for the original variables x and t is found by replacing c with c/η in (2.20),

$$c = \frac{3c}{\sqrt{2}q^2\sqrt{c^2 + 4\eta^2q^2}} + c_\infty, \quad (2.21)$$

where $c_\infty = 3a_0/\sqrt{2}q^2$.

For the symmetric case, $a_0 = 0$ and consequently $c_\infty = 0$. Equation (2.21) then has the solution $c = 0$ representing a stationary Ising front. This solution exists for all η values. When $\eta < \eta_c = 3/2\sqrt{2}q^3$, two additional solutions, $c = \pm 2q\sqrt{\eta_c^2 - \eta^2}$ appear, representing counterpropagating Bloch fronts. Figure 2.4 displays the corresponding pitchfork bifurcation.

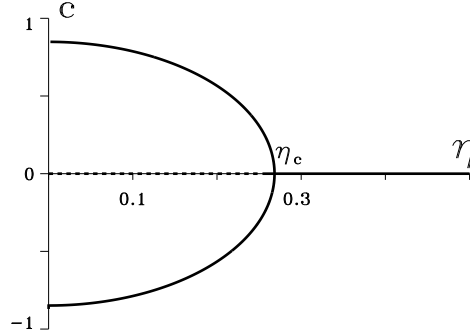


Figure 2.4: The NIB front bifurcation in the (c, η) plane for the symmetric case, $a_0 = 0$. The solid (broken) line represents a stable (unstable) branch of front solutions.

For the nonsymmetric case we solve (2.21) numerically. A plot of the solutions, $c = c(\eta)$, in the (c, η) plane yields the saddle-node bifurcation diagram shown in Figure 2.5. The bifurcation point, $\eta = \eta_c$, occurs for a smaller critical η value than the symmetric case, and the front that exists for $\eta > \eta_c$ is not stationary. We still refer to the two stable counterpropagating fronts beyond the bifurcation as Bloch fronts and to the single front that exists for $\eta > \eta_c$ as an Ising front.

Since $\eta^2 = \epsilon\delta$ the bifurcation point, $\eta = \eta_c$, defines a line in the $\epsilon - \delta$ plane, $\delta = \delta_F(\epsilon)$. For the symmetric case $\delta_F(\epsilon) = \eta_c/\epsilon = 9/8q^6\epsilon$. For the nonsymmetric case the bifurcation line was computed numerically. Figures 3.1 and 3.2 show the bifurcation lines for the symmetric and nonsymmetric cases respectively. These results for the bifurcation line are not valid for $\delta \sim \mathcal{O}(\epsilon)$ and smaller. In that regime we use a different approach as described in Section B.

2.5 Front Transitions

Dynamic transitions between the two counterpropagating fronts are possible near the NIB bifurcation. These front transitions are induced by perturbations on the system. The perturbations may

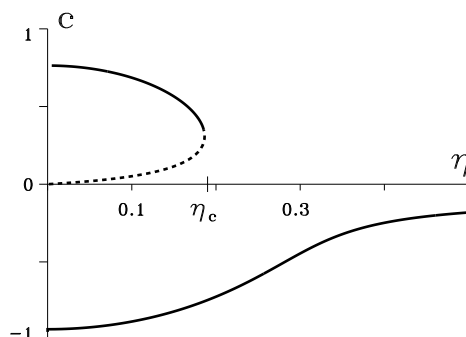


Figure 2.5: The NIB front bifurcation in the (c, η) plane for the nonsymmetric case, $a_0 = -0.1$. The solid (broken) line represents a stable (unstable) branch of front solutions.

be either intrinsic, like curvature (in two dimensions) and front interactions, or extrinsic, like an external convective field. Front transitions are important for analyzing the splitting domains (spot splitting), spiral breakup due to convective forces, oscillation of one and two dimensional domains, and the nucleation of spiral vortices.

The general form of the front velocity vs. perturbation relation is given by a multivalued curve as shown in Figure 2.6. This figure, typical near a NIB bifurcation, shows how realizable perturbations may drive the system past the knee of the relation and induce a transition from a rightward traveling front to a leftward traveling front. For a traveling pulse, this type of transition may destroy the pulse in the following way. Consider the case of zero perturbation in Figure 2.6. For a rightward propagating pulse the leading front is on the upper branch of the velocity-perturbation relation and the trailing front (or back) is on the lower branch. If the value of the perturbation is lowered in a portion of the domain, the leading front will undergo a transition when it reaches that location. The transition reverses the front's direction and sends it propagating towards the back. For δ sufficiently small or for fast fronts traveling wave parameters, two opposing fronts approaching each other annihilate (see B) and the pulse is destroyed.

In [36] we derive an order parameter equation for the dynamics of fronts under perturbations. This scalar equation has a double-well potential similar to the scalar diffusion equation (1.2) but this time each well represents a traveling wave solution. The resulting order parameter equation is gradient [37], implying that when the system is perturbed past the endpoint of a branch (thus losing one of the potential wells) a transition occurs to the other remaining (counterpropagating) solution.

In this section we show how the multivalued velocity vs. perturbation relation arises for both a convective perturbation and a nonuniform spatial value of the parameter a_0 . In Chapter 3 we will see how curvature provides a very similar effect by producing a multivalued speed vs. curvature relation. To demonstrate the effects of the multivalued relation we show how a pulse collapses due to a convective perturbation and how oscillating domains arise in systems with spatially nonuniform

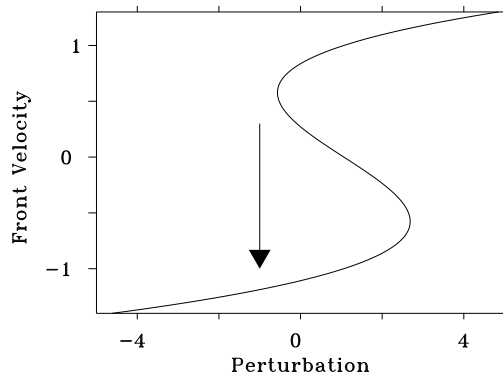


Figure 2.6: A typical front velocity vs. perturbation graph near a NIB bifurcation. The arrow shows the direction of a front transition from a rightward traveling front to a leftward traveling front

parameters.

2.5.1 Transitions Induced by Convection

First consider introducing a convective perturbation, J , to the one-dimensional model equations

$$\begin{aligned} u_t &= u - u^3 - v + u_{xx}, \\ v_t &= Jv_x + \epsilon(u - a_1v - a_0) + \delta v_{xx}. \end{aligned} \quad (2.22)$$

In a chemical system the term J might represent transport of ions due to an electric field or convective transport in a flow field. Often there is no reason to expect that each chemical species would convect differently in a flow field, but often the model is a reduction of a complex chemical system. When equations are eliminated from the original many species model, effective differential flows may occur when transport terms are renormalized [38].

In the traveling frame $\chi = x - ct$ with constant speed c , Eqs. (2.22) become

$$\begin{aligned} u_{\chi\chi} + cu_\chi + u - u^3 - v &= 0, \\ \delta v_{\chi\chi} + (c + J)v_\chi + \epsilon(u - a_1v - a_0) &= 0. \end{aligned} \quad (2.23)$$

Multiplying the v equation in (2.22) by the factor $\Delta(s, t) = c/(c + J)$ we obtain the following pair of equations,

$$\begin{aligned} u_{\chi\chi} + cu_\chi + u - u^3 - v &= 0, \\ \tilde{\delta}v_{\chi\chi} + cv_\chi + \tilde{\epsilon}(u - a_1v - a_0) &= 0, \end{aligned} \quad (2.24)$$



CHAPTER 2. PATTERNS IN ONE DIMENSION

where $\tilde{\delta} = \Delta\delta$ and $\tilde{\epsilon} = \Delta\epsilon$. These new equations describe a front propagating at speed c but in a *unperturbed* medium characterized by the new effective parameters $\tilde{\epsilon}$ and $\tilde{\delta}$.

In Section 2.4 we derived a relation for the front speed as a function of the system parameters. The speed of a front, c_0 , is given by

$$c_0 = F(c_0, \eta), \quad F(X, Y) = \frac{3X}{\sqrt{2}q^2\sqrt{(X^2 + 4q^2Y^2)}} + c_\infty, \quad (2.25)$$

with $\eta^2 = \epsilon\delta$, $q^2 = a_1 + 1/2$, and $c_\infty = 3a_0/\sqrt{2}q^2$. Using equation (2.25) and substituting the new parameters, $c_0 \rightarrow c$, $\epsilon \rightarrow \tilde{\epsilon}$, and $\delta \rightarrow \tilde{\delta}$, we obtain the speed of fronts in the perturbed system

$$c = F(c + J, \eta). \quad (2.26)$$

Figure 2.7 shows graphs of c vs. J for parameters deep in the Bloch regime (η large), near the NIB bifurcation, and far in the Ising regime (η small). Away from the bifurcation, in both the Ising and Bloch regimes, the relation is nearly linear. In the Ising regime there is a single solution and in the Bloch regime there are three, two representing the stable counterpropagating fronts and one representing the unstable front. Near the NIB bifurcation the c vs. J relation is *multivalued*. Finite perturbations may drive a front past the knee in the multivalued relation and induce a front transition thus reversing its direction of propagation.

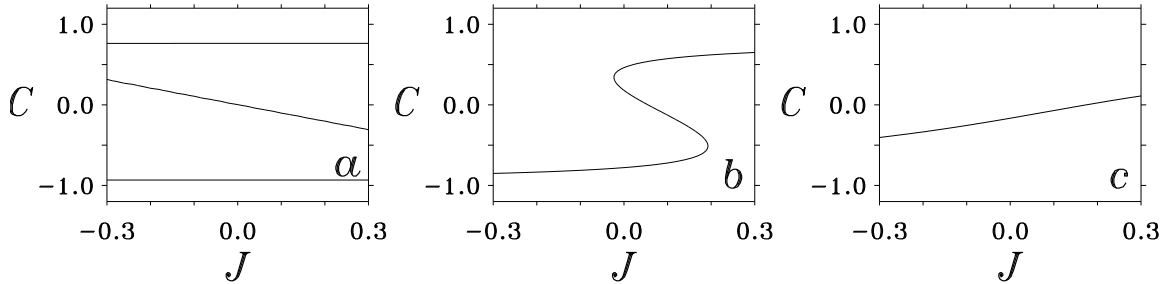


Figure 2.7: Front velocity, c , vs. convective perturbation, J : (a) deep in the Bloch regime, (b) near the NIB bifurcation, (c) deep in the Ising regime.

To demonstrate how fronts make transitions consider a c vs. J relation as shown in Fig. 2.8a. For zero perturbation both counterpropagating fronts exist but for values of J less than the endpoint of the upper branch ($J = J_c \sim -0.10$) only the single lower branch exists. If the domain of the equations has a region where the parameter J is less than J_c , rightward propagating fronts will make a transition there to leftward propagating fronts. Figure 2.9 shows a numerical experiment in which the distribution of the perturbation J is fixed to be that shown in Fig 2.8b. A rightward traveling front (Fig 2.9a) makes a transition when it reaches the region of negative J . A pulse solution propagates until the leading front makes a transition and annihilates the trailing back (Fig 2.9b) leading to pulse collapse.

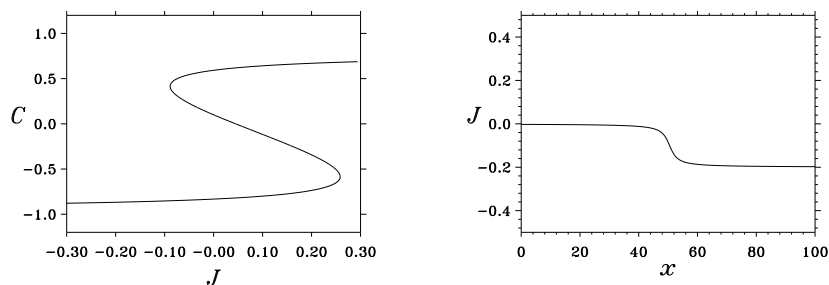


Figure 2.8: Parameters for the numerical simulations of Figure 2.9. (a) The c vs. J relation. (b) The nonuniform distribution of J in the domain.

2.5.2 Oscillating Domains

Another possible outcome of the multivalued c vs. J relation is the formation of oscillating fronts and pulses. The single valued curve in Fig. 2.10a represents the c vs J relation away from the NIB bifurcation in the Ising regime. At a fixed value of J , approximately $J = 0.1$, the front is stationary. For smaller J it propagates to the left and for larger J to the right. If the domain has a nonuniform distribution of J as in Fig. 2.10b, a front will make damped oscillations until it reaches the steady state position where J attains the value of the zero speed front as depicted in Fig. 2.11a.

If the c vs. J relation is multiple valued as in Fig. 2.12, the $c = 0$ front is unstable. Now the rightward traveling in the zero perturbation region makes a transition from the upper branch to the lower branch (arrow A) when it crosses the point in the domain where J is decreased (near $x = 50$). It then propagates to the left. When the front reaches the region where J returns to its original value it makes a transition back to the right propagating solution (arrow B). This motion persists to form an isolated oscillating front as shown in Fig. 2.11b.

2.5.3 Mechanisms for Front Transitions

Variation of the equation parameters can also produce multivalued relations for front velocity vs. perturbation. Fig. 2.13 shows plots of front velocity vs. the parameter a_0 deep in the Bloch regime, near the NIB bifurcation, and far into the Ising regime. Since this relation has the same multivalued form we expect that similar front transitions occur as well. The semiconductor model proposed in Section 1.3.1 has a similar nonuniform spatial dependence on a parameter.

Another important mechanism for inducing front transitions is interactions between two independent front structures. In B, Section 4.2, we find oscillating domains in a uniform system. The mechanism for the front transitions that reverse front propagation and produce the oscillations of Figs. B14a and B15a is a repulsive front interaction. Our hypothesis is that there is also a similar multivalued relation behind the interactions of fronts although we do not have analysis to show that yet.

Finally, as will be discussed in Section 3.1, small curvature perturbations on fronts produce a multivalued front velocity relation. In Chapter 3 we will show how this can lead to spot splitting

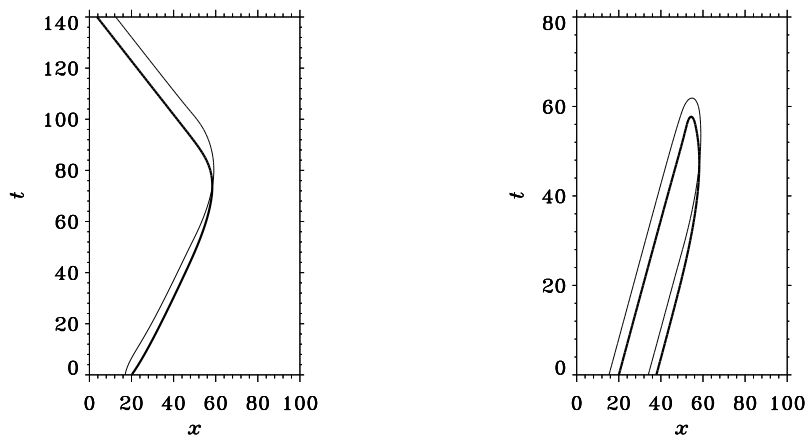


Figure 2.9: The effect of convective perturbations on the propagation of one-dimensional solutions. The thick line represents the position of the u fronts (defined to be $u = 0$) and the thin line is the position of the v fronts (at $v = 0$). (a) A front makes a transition from rightward to leftward propagating. (b) The leading front makes a transition and collides with the trailing front, thus annihilating the pulse.

and spiral turbulence.

2.6 “Spatiotemporal Oscillations in a Semiconductor Étalon”

The analyses and results of this section are presented in Paper C, “Spatiotemporal oscillations in a semiconductor étalon”. The following is a summary of the main results.

This paper contains a study of the semiconductor model of Section 1.3.1. Important steps were the scaling of the model equations and the construction of a code to numerically integrate the scaled system.

An significant feature of the model is that the input intensity parameter, I_{in} , of Equation (C3) is not uniform but instead Gaussian shaped (Equation (C7)). For this reason the system has spatially nonuniform parameter dependence through the term $I_c(N, T, x)$. We considered this system by analyzing the isoclines as they referred to each point in space, *eg.* the center of the system might correspond to an oscillatory system while the tails were monostable (and excitable). When variations of the spatial dependence of I_{in} are of the same order as the width of a typical pulse solution, as might be in a typical experimental setup, this type of analysis breaks down and a different approach to characterize the dynamics is used (see Section B of Paper C).

This approach had some success in explaining two interesting phenomena discovered in the



CHAPTER 2. PATTERNS IN ONE DIMENSION

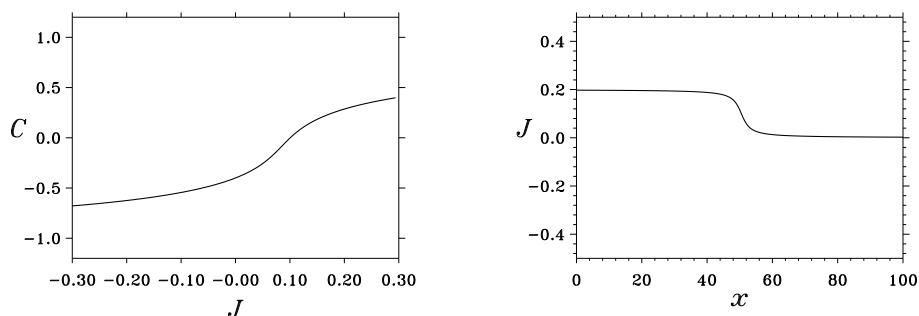


Figure 2.10: (a) The c vs. J relation for the case of damped oscillations to a stationary front and (b) The nonuniform distribution of J in the domain

numerical simulations, “whole-beam oscillations” and “edge oscillations”. Whole beam oscillations, shown in Figure C7, represent a nonuniform parameter version of an oscillatory system; the center of the system is of oscillatory type and the edges are monostable. A pulse is found to first spontaneously form and then contract until the pulse collapses. Edge oscillations occur for slightly different parameters where the pulse expands and contracts periodically as shown in Figure C17.

In the time since this paper was published we have found that oscillations can occur due to nonuniform parameter distributions near the NIB bifurcation. In the previous Section 2.5 we showed how a nonuniformity of the parameter a_0 can lead to oscillating, or breathing, domains. It would be interesting to check to see if the nonuniformity of the input beam intensity, I_{in} in this model, has the same effect.

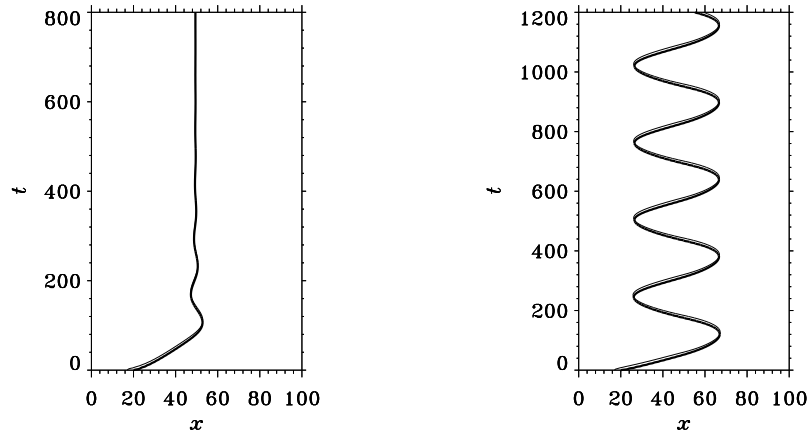


Figure 2.11: The effect of convective perturbations on the dynamics of single fronts. The thick line represents the position of the u fronts (defined to be $u = 0$) and the thin line is the position of the v fronts (at $v = 0$). (a) A single front undergoes damped oscillations to a stationary solution. (b) A single front maintains steady oscillations.

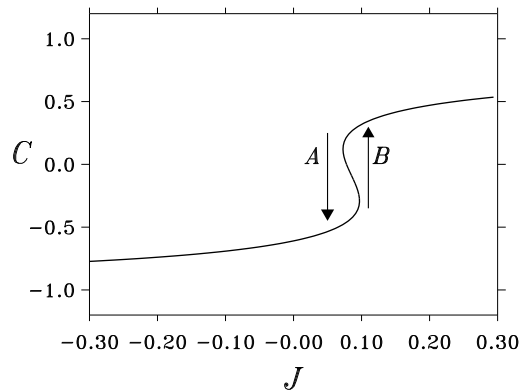


Figure 2.12: The c vs. J relation for the case of an oscillating front

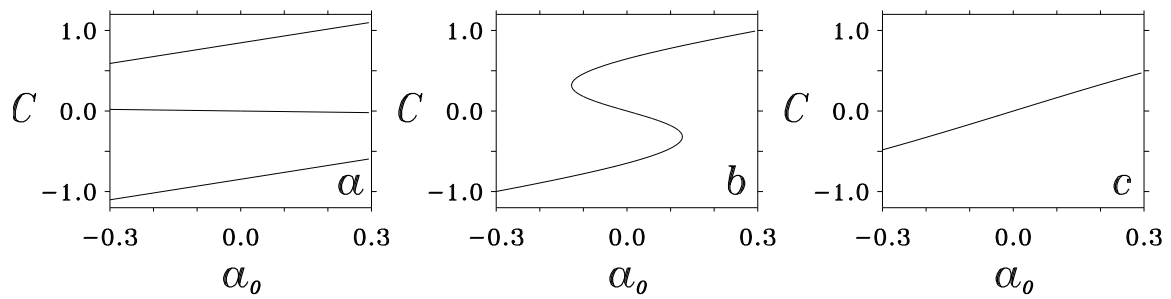


Figure 2.13: Front velocity, c , vs. the parameter a_0 : (a) deep in the Bloch regime, (b) near the NIB bifurcation, (c) deep in the Ising regime.



Chapter 3

Patterns in Two Dimensions

Labyrinthine patterns, spot replication, and spiral wave turbulence are all examples of complex spatial and spatiotemporal patterns exhibited in two-dimensional reaction-diffusion systems. Labyrinthine, or sometimes called lamellar, patterns have been observed in a variety of gradient systems [37] including garnet layers [39], ferrofluids [40], and block copolymers [41, 42]. Recently they also were found in the bistable FIS (ferrocyanide-iodate-sulfite) reaction [22]. This nongradient system also exhibits spot replication and spiral turbulence [23].

Much of this phenomenology can be understood in terms of two key front instabilities: an instability to transverse perturbations reminiscent of the Mullins-Sekerka instability in solidification fronts [43], and a Nonequilibrium Ising-Bloch (NIB) front bifurcation [34]. Beyond the transverse instability and deep in the Ising regime labyrinthine patterns may develop when small disturbances on planar Ising fronts grow and fill the system through fingering and tip splitting. In the vicinity of the NIB bifurcation intrinsic perturbations, such as curvature, may drive dynamic transitions between the two counterpropagating fronts and lead to spot splitting and spiral breakup [36].

In this Chapter we focus on the regime $\epsilon/\delta \ll 1$ of Eqs. (1.10). In Section 3.1 we derive the boundaries for the transverse instability. Next we demonstrate numerically the instability of planar Ising fronts to transverse perturbations. With suitable initial conditions we find either stationary labyrinthine patterns (Section 3.2) or spot-splitting (Section 3.3). In Section 3.4 the transverse instability is shown to lead to spiral turbulence; the continuous creation and destruction of spiral vortex pairs. Other mechanisms can also produce spiral turbulence as shown in Section 3.5. Finally in Section 3.6 we show how an external convective field can cause the breakup of a regular spiral pattern.

3.1 Transverse Instability

For δ sufficiently large, planar front solutions may become unstable to transverse perturbations [44, 45, 46]. To study the transverse instabilities of the various front solutions we change from the fixed coordinate system to a coordinate system moving with the front. Let $\mathbf{X} = (X, Y)$ be the position vector of the front represented by the $u = 0$ contour line. The moving coordinate frame (r, s) is



CHAPTER 3. PATTERNS IN TWO DIMENSIONS

defined by the relation

$$\mathbf{x} = (x, y) = \mathbf{X}(s, t) + r\hat{\mathbf{r}}(s, t), \quad (3.1)$$

with the coordinate s parameterizing the direction along the front, and

$$\hat{\mathbf{r}} = \frac{Y_s \hat{\mathbf{x}} - X_s \hat{\mathbf{y}}}{\sqrt{X_s^2 + Y_s^2}}, \quad (3.2)$$

the unit vector normal to the front (the subscript s denotes partial derivatives with respect to s). We assume the front radius of curvature is much larger than $l_v = \sqrt{\delta/\epsilon}$, the scale of v variations across the front. We also assume the curvature varies slowly both along the front direction and in time. With these assumptions Eqs. (1.10) assume the form

$$\begin{aligned} u_{rr} + (c_r + \kappa)u_r + u - u^3 - v &= 0, \\ \delta v_{rr} + (c_r + \delta\kappa)v_r + \epsilon(u - a_1v - a_0) &= 0, \end{aligned} \quad (3.3)$$

where $\kappa(s, t) = X_s Y_{ss} - Y_s X_{ss}$ is the front curvature, and $c_r(s, t) = \mathbf{X}_t \cdot \hat{\mathbf{r}}$ is the front normal velocity.

Multiplying Eqs. (3.3) by the factor $\Delta(s, t) = (c_r + \kappa)/(c_r + \delta\kappa)$ gives

$$\begin{aligned} u_{rr} + (c_r + \kappa)u_r + u - u^3 - v &= 0, \\ \tilde{\delta}v_{rr} + (c_r + \kappa)v_r + \tilde{\epsilon}(u - a_1v - a_0) &= 0, \end{aligned} \quad (3.4)$$

with $\tilde{\epsilon} = \epsilon\Delta$ and $\tilde{\delta} = \delta\Delta$. This system is exactly of the same form as Eqs. (2.9) for a planar ($\kappa = 0$) front propagating at constant speed, $c_r + \kappa$, in the normal direction, $\hat{\mathbf{r}}$, except the original parameters ϵ and δ are replaced by effective parameters $\tilde{\epsilon}$ and $\tilde{\delta}$ [47]. The front bifurcation formula derived in Section 2.4 can now be applied to show the effects of curvature on the front velocity. Using Eq. (2.21) with c replaced by $c_r + \kappa$ and η by $\tilde{\eta} = \eta\Delta$ we obtain an implicit relation for the normal front velocity in terms of its curvature,

$$c_r + \kappa = \frac{3(c_r + \delta\kappa)}{\sqrt{2}q^2[(c_r + \delta\kappa)^2 + 4\eta^2q^2]^{1/2}} + c_\infty. \quad (3.5)$$

Equation (3.5) can be used to study the stability of the planar fronts to transverse perturbations. We look for a linear velocity curvature relation,

$$c_r = c_0 - d\kappa + \mathcal{O}(\kappa^2), \quad (3.6)$$

valid for small curvature. Here $c_0(\eta)$ is the speed of a planar front satisfying (2.21). A positive (negative) sign of the coefficient d implies stability (instability) to transverse perturbations. Inserting (3.6) into the expression for the front speed, keeping only linear terms, we find,

$$d = \frac{1}{\alpha} + \left(1 - \frac{1}{\alpha}\right) \delta, \quad \alpha = 1 - \frac{c_0 - c_\infty}{c_0} \left(1 - \frac{2q^4}{9}(c_0 - c_\infty)^2\right). \quad (3.7)$$



CHAPTER 3. PATTERNS IN TWO DIMENSIONS

For each planar solution branch, $c_0 = c_0(\eta)$, the condition $d = 0$ defines a line in the $\epsilon - \delta$ plane where the corresponding planar front branch undergoes a transverse instability. Setting $d = 0$ for the symmetric case ($a_0 = 0$), the Ising and Bloch fronts become unstable to transverse modulations when $\delta > \delta_I(\epsilon) = \frac{8}{9}q^6\epsilon$ and $\delta > \delta_B^\pm(\epsilon) = 3/2\sqrt{2}q^3\sqrt{\epsilon}$, respectively. The transverse instability boundary and the front bifurcation line, $\delta_F(\epsilon) = 9/8q^6\epsilon$, are shown in Fig. 3.1. Figure 3.2 shows the transverse instability boundaries and the front bifurcation line for a typical nonsymmetric case. Note that the lines corresponding to the two Bloch fronts, denoted by δ_B^\pm , are not degenerate as in the symmetric case.

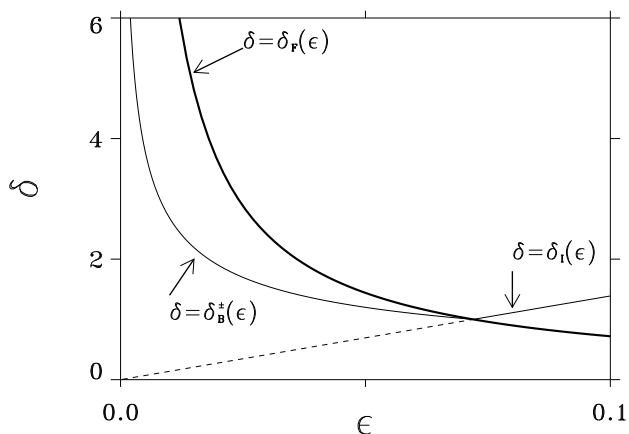


Figure 3.1: The NIB bifurcation and the transverse instability lines in the $\epsilon - \delta$ parameter plane for the symmetric case ($a_0 = 0$). The front bifurcation, $\delta = \delta_F(\epsilon)$, is indicated by the thick line. The transverse instabilities are indicated by the thin lines, $\delta = \delta_I(\epsilon)$ for Ising fronts, and $\delta = \delta_B^\pm(\epsilon)$ for Bloch fronts.

The two instabilities presented above provide a guide to exploring pattern types in the $\epsilon - \delta$ plane. Deep in the Ising regime there exists only one type of front and no traveling pulses or waves are expected [Paper B]. Instead, stationary patterns may develop: ordered stripes below the transverse instability, and labyrinthine patterns above it. Far into the Bloch regime, where there is coexistence of counterpropagating fronts, traveling stripes and spiral waves appear. They are smooth below the transverse instability and develop ripples above it. The transition between these two regimes is not sharp. There exists an intermediate region, including the NIB bifurcation line, where complex spatio-temporal patterns such as replicating spots and spiral turbulence are found.

The key to understanding these complex behaviors is the multivalued form of the velocity-curvature relation near the NIB bifurcation. Figure 3.3 shows typical solution curves of Eq. (3.5). The multivalued velocity-curvature relation near the NIB bifurcation (Fig. 3.3b) unfolds to a single valued relation far in the Ising regime (Fig. 3.3a), or folds even further to form three effectively dis-

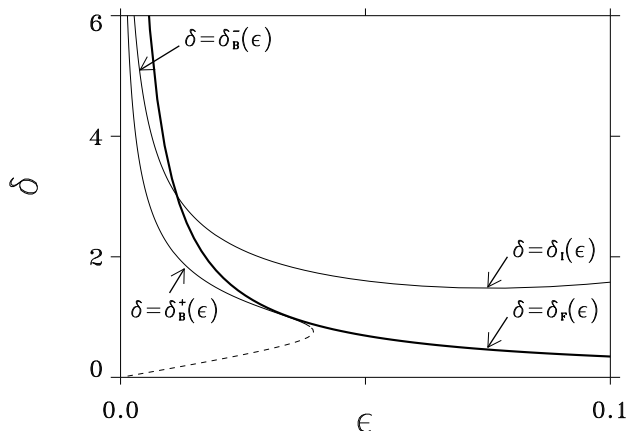


Figure 3.2: The NIB bifurcation and the transverse instability lines in the $\epsilon - \delta$ parameter plane for the nonsymmetric case ($a_0 = -0.1$). The front bifurcation, $\delta = \delta_F(\epsilon)$, is indicated by the thick line. The transverse instabilities are indicated by the thin lines, $\delta = \delta_I(\epsilon)$ for Ising fronts, and $\delta = \delta_B^\pm(\epsilon)$ for Bloch fronts.

connected linear branches deep in the Bloch regime (Fig. 3.3c). The same front transitions discussed in Section 2.5 occur, but now with curvature as the perturbation instead of an external field. As in the one-dimensional example such transitions reverse the direction of front propagation. When occurring locally in two-dimensions they nucleate spiral-vortex pairs and may lead to spot splitting and spiral turbulence.

Most studies of traveling waves in excitable and bistable media [9, 10, 33] have assumed a linear velocity-curvature relation, $c_r = c_0 - d\kappa$. The linear relation is valid deep into the Bloch regime ($\eta \ll \eta_c$) and not near the NIB bifurcation (see also [48]) with the exception of the special case $\delta = 1$. There, $d = 1$ and the velocity is simply $c_r = c_0 - \kappa$, where $c_0(\eta)$ satisfies (2.21). Figure 3.3e shows a typical velocity-curvature relation in the Bloch regime when $\delta = 1$. The three linear branches correspond to the three solutions of Eq. (2.21). Approaching the NIB bifurcation when $\delta = 1$, the two upper branches coalesce leaving only the single lower branch in the Ising regime. Near the NIB bifurcation for $\delta > 1$ the upper branch terminates at negative curvature values (Fig. 3.3d) while for $\delta < 1$ it terminates at positive curvature (Fig. 3.3f).

3.2 Labyrinthine Patterns

Far into the Ising regime and beyond the transverse instability line, $\delta > \delta_I(\epsilon) = \frac{8}{9}q^6\epsilon$, front shapes meander, grow fingers, and split at the tips. This behavior can be understood using the velocity-curvature relation deep in the Ising regime, as depicted in Fig. 3.4c. The positive slope of this



relation over a wide range of curvature implies that front portions with higher curvature propagate faster, forming fingers. It also implies that the transverse instability remains effective even at the highly curved fingertips. This leads to tip splitting.

Figure 3.5 shows the evolution of a stripe domain in the Ising regime above the transverse instability boundary and corresponding to the velocity-curvature relation in Fig. 3.4c. The initial stripe is perturbed transversely along the middle part. The perturbation grows, forms a meandering stripe, and then undergoes fingering and tip splitting. A final stationary labyrinth results when the pattern fills the entire domain.

Notice the final pattern in Fig. 3.5d is connected since there were no domain fusion events during the evolution. Domain fusion is avoided by the repulsive front interactions (due to the diffusive damping of v in the region between approaching fronts [B]). Closer to the front bifurcation the front speeds are higher (see Fig. 2.5) and the repulsive interactions may not be strong enough to prevent fusion. As a result the eventual stationary pattern may contain disconnected domains.

Similar labyrinthine patterns have been observed in the bistable FIS reaction [22]. Our interpretation is that these patterns occur in the Ising regime where the single front structure corresponds to a high pH state invading a low pH state.

3.3 Single Spot Dynamics

Closer to the NIB bifurcation the nonlinearity of the velocity-curvature relation becomes important. Consider an up state disk expanding radially outward. Depending on the system parameters several scenarios for evolution are possible. Deep enough into the Ising regime, where the velocity-curvature relation is still single valued (see Fig 3.4a), a stationary disk solution exists. The disk has radius $1/\kappa_0$, where $c_r(\kappa_0) = 0$, and is stable to uniform expansions and contractions because the velocity-curvature relation has positive slope at $c_r = 0$ (it might be unstable, however, to transverse perturbations [45]).

Still closer to the front bifurcation (but in the Ising regime) the velocity-curvature relation becomes multivalued, and the slope at $c_r = 0$ negative, as illustrated in Fig. 3.4b. The stationary disk is no longer stable to expansions and contractions and a breathing disk solution appears [45]. To understand this breathing motion, note first that the boundary of an expanding disk corresponds to a front lying on the upper branch in Fig. 3.4b. As the disk expands the front curvature decreases. When the curvature falls below the value where the upper branch terminates a transition to the lower branch takes place. The disk stops expanding and starts contracting. The curvature increases until the endpoint of the lower branch is reached and a transition back to the upper branch occurs. As a result the disk stops contracting and begins expanding again. These oscillations are similar to those found in one-dimensional domains [B] [49, 50] with front interactions playing the role of curvature in inducing front transitions [36].

To verify these expectations we studied numerically Eqs. (1.10) in polar coordinates assuming circularly symmetric front solutions (to avoid transverse instabilities). Such solutions satisfy

$$u_t = u_{rr} + \frac{1}{r}u_r + u - u^3 - v, \quad (3.8)$$



$$v_t = \delta v_{rr} + \frac{\delta}{r} v_r + \epsilon(u - a_1 v - a_0). \quad (3.9)$$

They represent circular fronts with curvatures $\kappa(t) = 1/r_0(t)$, where $r_0(t)$ solves $u(r_0, t) = 0$. Figures 3.6 and 3.7 show the curvatures of up state disks as functions of time for parameters pertaining to Figs. 3.4a and 3.4b respectively. A single valued (multivalued) velocity-curvature relation leads to a stationary (oscillatory) asymptotic state.

In fully two-dimensional systems oscillating disks might be unstable to non-circularly symmetric perturbations. Consider an expanding disk perturbed to an oval shaped domain as shown in Fig. 3.8a. The parameters chosen pertain to a velocity-curvature similar to the one in Figure 3.4b. As the domain expands the flatter portions of its boundary are the first to reach the end of the upper branch and undergo front transitions. These portions then propagate towards one another, annihilate, and split the domain as shown in Figs. 3.8b and 3.8c. The crossing points of the $u = 0$ and $v = 0$ contour lines indicate the cores of spiral vortices. Note that the splitting process involves the creation and the subsequent annihilation of two spiral-vortex pairs. A successive splitting is shown in Fig. 3.8d. The asymptotic state in this case is a disordered stationary pattern with many disconnected domains. Remnants of the unstable breathing motion are often seen when the split spots first contract, then approach a minimum size and start expanding. Both spot splitting and the persistence of small spots have been observed recently by Lee *et al.* in the FIS reaction [23, 24].

3.4 “From Labyrinthine Patterns to Spiral Turbulence”

The analyses and results of this section are described in Paper D, “From labyrinthine patterns to spiral turbulence.” The following is a summary of the main results.

Further approach to the NIB bifurcation results in disordered dynamic patterns where spiral vortices nucleate and annihilate repeatedly. We refer to such a state as spiral turbulence. The nucleation of spiral-vortex pairs results from local front transitions, very much like in spot splitting except the mechanisms that drive the transitions are different and depend on the system parameters.

Paper D is a study of how the transverse instability can lead to both labyrinthine patterns and spiral turbulence. Far into the Ising regime, labyrinthine patterns form when planar fronts are destabilized. Beyond the NIB bifurcation spiral waves may form. Near the NIB bifurcation, spirals waves break due to both the transverse instability and the formation of highly curved cusp regions.

This paper is where we first derive the boundaries for the transverse instability as shown in Section 3.1 (see Figs. 3.1 and 3.2). The transverse instability boundaries and front bifurcation line divide the $\epsilon - \delta$ parameter plane into regions of different pattern behaviors. First consider the region below the transverse instability boundaries, $\delta < \delta_B^\pm$. In the Ising regime ($\eta > \eta_c$), where there is a single isolated front solution, we find stationary stripe solutions. If δ is small, below the critical value for formation of stationary domains (see μ_{st} in Figure 18 of [B]), no stationary domains form and the system goes to the uniform up-state or down-state. In the Bloch regime ($\eta < \eta_c$), we find traveling and spiral waves.

Above the transverse instability boundaries we find different behavior. The stationary stripes in the Ising regime are unstable to perturbations and grow to form labyrinthine patterns as already



CHAPTER 3. PATTERNS IN TWO DIMENSIONS

seen in Section 3.2. Near the front bifurcation line the uniform spiral waves break and new spiral waves are continuously nucleated and destroyed.

Figure D4 shows the development of spiral turbulence from a single stripe domain. For the parameters of this simulation both the front and the back of the initial stripe are unstable to transverse perturbations. The stripe first breaks into pieces that each form part of a new spiral wave. The new spiral waves are also unstable and the system evolves to a state of continuous birth and death of spiral waves.

In addition to the transverse instability, the formation of highly curved front regions also plays a role in the development of spiral turbulence. When two up-state domains merge, often cusp-like regions of high curvature form between them as in Fig. D5a. The transverse instability and negative curvature cusp regions both drive fronts to the end of a solution branch and induce transitions. The transitions locally reverse the direction of front propagation and cause the domain to be cut into disjoint pieces. Figure D5 shows this process in detail. The dark and light shadings indicate regions of the up-state and down-state of u . The thick line is the zero contour of the u field and the thin line is the zero contour of the v field. An original single cusp-like structure is formed in a rightward propagating front (Fig. D5a). It grows (Fig. D5b) and nucleates a pair of spiral vortices as crossings of the zero contours (Fig. D5c). Finally the domain is cut and two new spiral tips are formed (Fig. D5d).

The simulation was continued to $t = 6000$ without any qualitative change in the solution. Figure 3.9 shows a plot of the number of vortices as a function of time. After an initial period of sharply increasing number of vortices, the number fluctuates between approximately 30 and 70. Since the system is small the fluctuations are large compared with the average number. Although the solution maintains the same qualitative form until $t = 6000$, the uniform states, (u_-, v_-) and (u_+, v_+) , are always solutions to Eqs. (1.10) and it is possible that eventually the system might evolve to either one of those states.

3.5 Spiral Turbulence Revisited

As we have seen in the previous section, for δ sufficiently large, the transverse instability plays a dominant role in inducing front transitions that lead to spiral turbulence. Figures 3.10 and 3.11 show spiral turbulence for smaller δ values. In this parameter regime front interactions are the major driving force. Figures 3.4f and 3.4g show the corresponding velocity-curvature relations for Figs 3.10 and 3.11. In both figures the upper branches terminate at positive curvature values. Processes reducing the curvature of fronts on these branches past the endpoints cause transitions to the lower front branches. As we have seen in the previous section, single noncircularly symmetric domains may undergo such transitions and split. In the presence of nearby domains, however, repulsive front interactions accelerate domain splitting by flattening out approaching curved fronts. Frames *d, e, f* of Figures 3.10 and 3.11 show local front transitions and splitting driven by front interactions (see the regions indicated by the arrows). These processes are strikingly similar to those observed in the FIS reaction [24]. Front interactions may also cause spiral-vortex nucleation and splitting by directly inducing front transitions. Reflection of one-dimensional fronts provides an example of front interactions leading to front transitions [B]. The spiral-vortex nucleations in



Figs. 3.10 and 3.11 are likely to result from both mechanisms.

The patterns in Fig. 3.10 differ from those in Fig. 3.11 in a few respects. The initial conditions in both simulations are the same but the subsequent spiral breakup is different. In Figure 3.10 most of the spiral wave disappears as the weakly curved front away from the core undergoes a front transition. In Fig. 3.11 the weakly curved part of the spiral survives longer until front interactions or interactions with the boundaries come into play. This is because the upper branch of the the velocity-curvature relation pertaining to Fig. 3.11 terminates at a lower curvature value than that of Fig. 3.10 (see Figs. 3.4f and 3.4g). Another difference is the prevalence of more spots in the patterns of Fig. 3.10. This is partly because domain fusions are avoided in Fig. 3.10 but occasionally take place in Fig. 3.11 (closer to the NIB bifurcation, front speeds are higher and domain fusions are more likely).

3.6 Spiral Breakup by an External Convective Field

A convective perturbation may also cause the breakup of a uniformly rotating spiral wave. Experiments on the Belousov-Zhabotinsky reaction in a Petri dish [11] show target and spiral waves, but when the cover of the dish is removed convective motion due to evaporation sets up Bénard cells in the layer. The onset of convective motion destroys the ordered spiral state [51, 52]. The resulting disordered state returns to an ordered state when the cover is replaced.

Adding a convection term to the model equations (1.10) we obtain

$$\begin{aligned} u_t &= u - u^3 - v + \nabla^2 u, \\ v_t &= \epsilon(u - a_1 v - a_0) + \mathbf{J} \cdot \nabla v + \delta \nabla^2 v, \end{aligned} \tag{3.10}$$

where \mathbf{J} is an external vector field. We already considered in Section 2.5 the effects of such a perturbation in a one dimensional system where $\mathbf{J} = J\hat{x}$. We found that near the NIB bifurcation the velocity vs. J relation was multivalued and that perturbations could induce transitions from rightward propagating to leftward propagating fronts. The result was that traveling pulses might collapse when the leading front, on one branch of the relation, makes a transition, while the trailing front, on the other branch, does not.

Now let \mathbf{J} represent a two dimensional convection pattern in the form of hexagonal Bénard cells with the system parameters tuned to produce the velocity vs. J relation as in Figure 2.8. For a propagating stripe of up-state domain, such as the arm of a spiral, the leading front is on the upper branch of the velocity vs. J relation and the trailing front is on the lower branch. Notice, at $J = 0$, that the leading front is close to the end of the upper branch (in the negative J direction) but the speed of the front on the lower branch is barely affected by changes in J . When the stripe propagates through the hexagonal pattern alternating portions of the leading front feel convective perturbations in the opposite direction of propagating, i.e. regions where $J = \mathbf{J} \cdot \hat{\mathbf{n}} < 0$. If the magnitude is large enough, the leading front will make a transition, nucleating a spiral vortex pair at each Bénard cell.

Figures 3.12 and 3.13 show the breakup of a spiral wave in a hexagonal convective field. The



CHAPTER 3. PATTERNS IN TWO DIMENSIONS

convective field is given by $J = \nabla\phi$, where

$$\phi = A \sum_{i=1}^3 \cos(\mathbf{q}_i \cdot \mathbf{x}), \quad (3.11)$$

$$\mathbf{q}_1 = (Q, 0), \quad \mathbf{q}_2 = (-Q/2, \sqrt{3}Q/2), \quad \mathbf{q}_3 = (-Q/2, -\sqrt{3}Q/2). \quad (3.12)$$

When the convective field is switched on, after Frame *a* of Figure 3.12, the spiral wave breaks at the Bénard cells, forming new spiral vortex pairs. Figure 3.13 provides a closer look at the nucleation process near one cell.

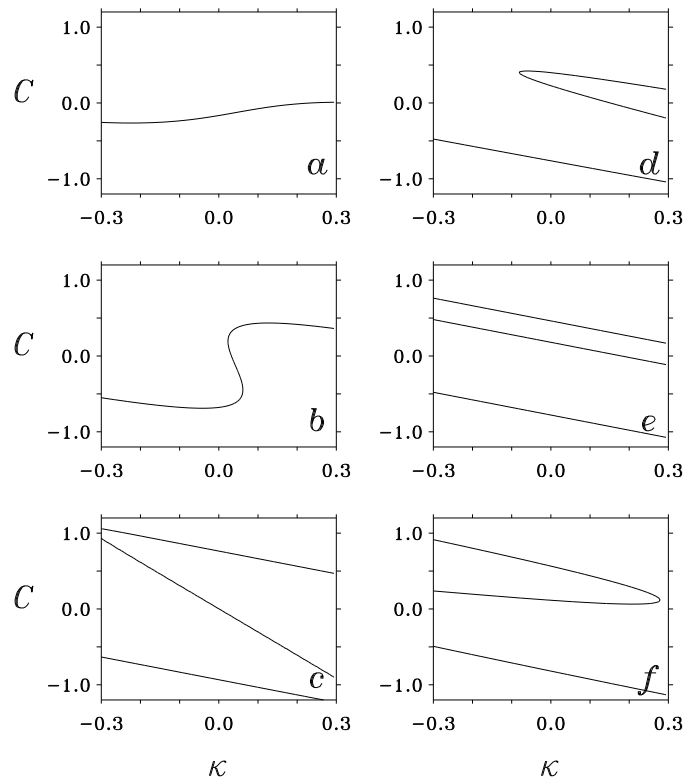


Figure 3.3: Front velocity, c , vs. curvature, κ . (a) Deep in the Ising regime. (b) Near the NIB bifurcation. (c) Deep in the Bloch regime. In the Bloch regime near the NIB bifurcation: (d) $\delta > 1$, (e) $\delta = 1$, (f) $\delta < 1$.

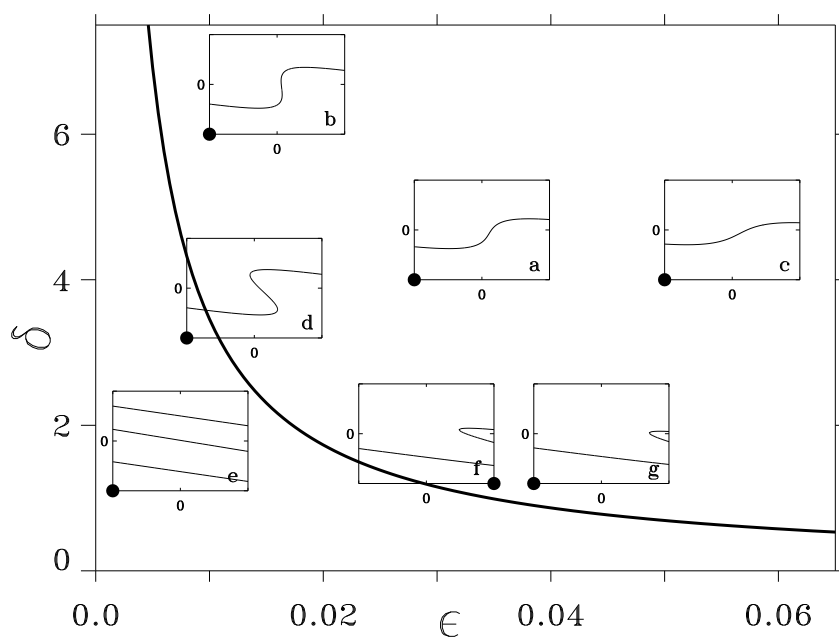


Figure 3.4: A map of the velocity vs. curvature relation plane. The thick line represents the front bifurcation for $a_0 = -0.1$ and the insets display c vs. κ for the point indicated by the solid circle. The axis scales for the insets are the same as in Fig. 3.3.

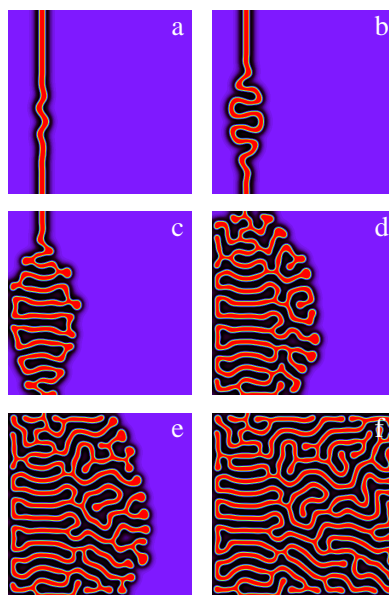


Figure 3.5: The evolution of an initially perturbed stationary stripe in the Ising regime above the transverse instability line (see Figure 3.4c). The dark and light regions correspond to the up and down states respectively. The frames a, b, c, d, e, f pertain to times $t = 100, 525, 1100, 1900, 2675, 5000$. The computational parameters are $a_1 = 2.0$, $a_0 = -0.1$, $\epsilon = 0.05$, $\delta = 4.0$ on a domain of $0 \leq x \leq 400$, $0 \leq y \leq 400$.

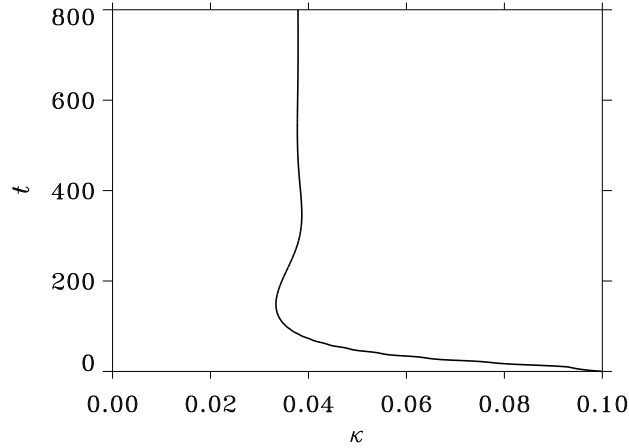


Figure 3.6: Curvature, κ , vs. time for a disk shaped domain. Far in the Ising regime (Figure 3.4a) a stationary disk pattern is reached. Computational parameters: $a_1 = 2.0$, $a_0 = -0.1$, $\epsilon = 0.028$, $\delta = 4.0$.

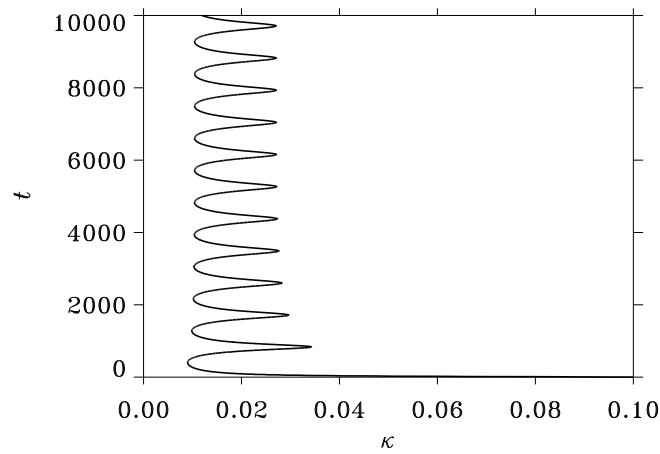


Figure 3.7: Curvature, κ , vs. time for a disk shaped domain. Near the NIB bifurcation (Figure 3.4b) oscillations set in. Computational parameters: $a_1 = 2.0$, $a_0 = -0.1$, $\epsilon = 0.01$, $\delta = 6.0$.

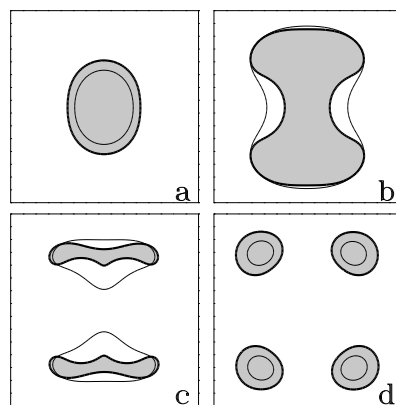


Figure 3.8: Spot splitting of an oval shaped domain. The shaded (light) region corresponds to the up (down) state and the thick (thin) line represents the contour of the $u = 0$ ($v = 0$) field. Frames a, b, c, d pertain to times $t = 80, 240, 280, 340$. Local front transitions occur at the flatter portions of the front. They are accompanied by nucleation of vortex pairs, and followed by domain splitting. Computational parameters: $a_1 = 2.0, a_0 = -0.15, \epsilon = 0.014, \delta = 3.5$.

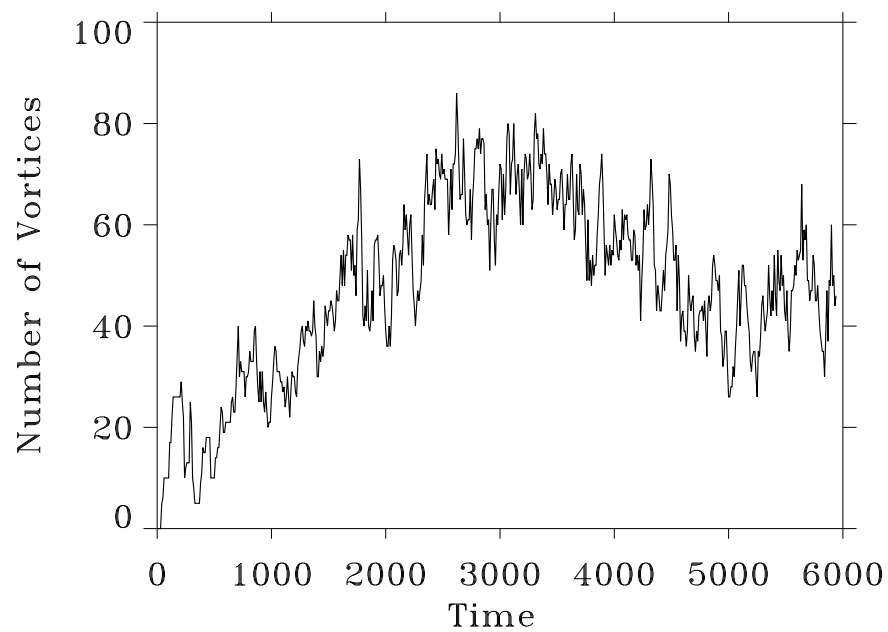


Figure 3.9: Number of vortices vs. time for the simulation in Figures 4 and 5 of Paper D. A vortex is defined by the crossing of the $u = 0$ and $v = 0$ contours.

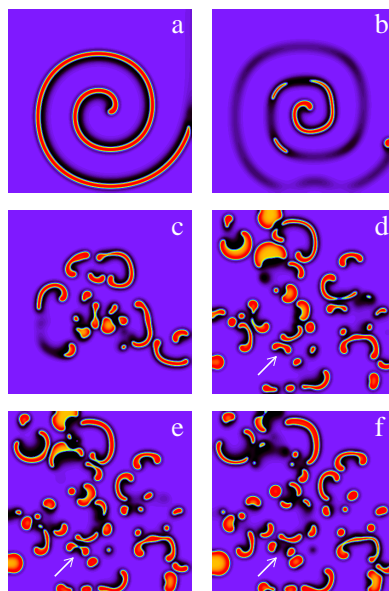


Figure 3.10: Spiral breakup for the velocity vs. curvature relation of Figure 3.4g. The frames a, b, c, d, e, f represent the solution at times $t = 60, 640, 1540, 3760, 3780, 3800$ respectively. The computational parameters are $a_1 = 2.0$, $a_0 = -0.10$, $\epsilon = 0.0375$, $\delta = 1.2$ on a domain of $0 \leq x \leq 400, 0 \leq y \leq 400$. For a more detailed description see the text.

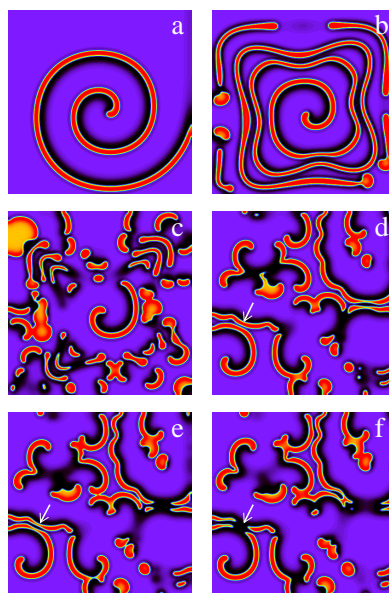


Figure 3.11: Spiral breakup for the velocity-curvature relation of Figure 3.4f. The frames a, b, c, d, e, f represent the solution at times $t = 80, 620, 900, 1890, 1900, 1910$ respectively. The computational parameters are the same as Figure 3.10 with $\epsilon = 0.035$. For a more detailed description see the text.

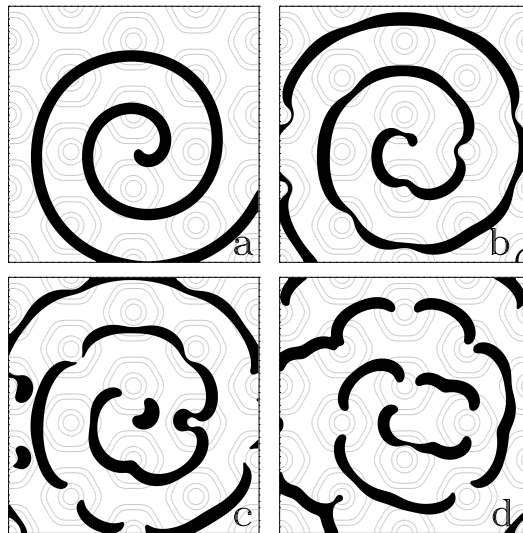


Figure 3.12: Breakup of a spiral wave induced by a hexagonal convective pattern. The light and dark regions correspond to down and up states, respectively. The dotted curves denote contours of constant convection speed. The convection flow direction is outward from the centers of the hexagons. Frame *a* is the unperturbed spiral wave and frames *b*, *c*, *d* are taken at times $t = 100, 140, 220$ from the onset of the convective pattern. Parameters used: $a_0 = -0.1$, $a_1 = 2.0$, $\epsilon = 0.032$, $\delta = 0.9$, $A = 1.59$ and $Q = 0.06283$.

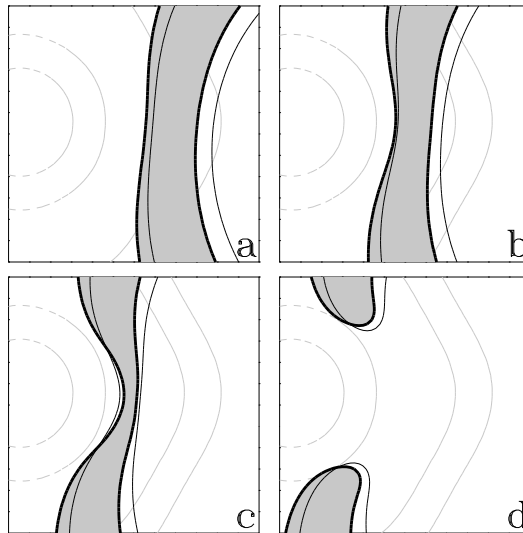


Figure 3.13: A closer look at a typical breakup process in Figure 3.12. The thick (thin) lines are contours of $u = 0$ ($v = 0$). The direction of front propagation follows from the rule that the $v = 0$ contour always lags behind the $u = 0$ contour. The frames a, b, c, d pertain to times $t = 140, 160, 180, 200$. They show a local front transition, accompanied by the nucleation of a vortex pair (the crossing points of the contour lines), and the breakup of the up state domain. Parameters are the same as in Figure 3.12.



Chapter 4

Numerical Methods

Numerical simulations of Eqs. (1.10) were crucial to the development and testing of the ideas presented in this dissertation. This Chapter provides a description of methods and algorithms used for numerically computing the one-dimensional and two-dimensional solutions. Although Eqs. (1.10) are often viewed as a reduction from a more complicated set of equations they are still non-trivial to solve in large domains and for long times. In one dimension most solutions could be computed quite easily on small workstations using general methods for PDE's and packaged software tools. Two-dimensional simulations, typically on grid sizes of 400×400 , required more careful schemes to be feasible on the same class of machines.

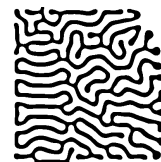
The numerical solutions were computed using the method of lines approach for partial differential equations [55, 56]. The method of lines decouples the discretization of the spatial and temporal operators into independent problems. The spatial derivatives were represented on uniform grids with finite difference approximations and the resulting set of coupled ordinary differential equations solved by a suitable time discretization; depending on the parameter regime either an explicit or implicit method. The explicit methods are appropriate for situations where the time scales are not widely varying (ϵ is not too small or large compared with 1) and when the diffusion is not too big (δ of $\mathcal{O}(1)$ or smaller). They were used to compute the traveling waves and spiral waves in the Bloch regime. The implicit methods were used for the computation of slowly varying patterns such as the formation of stationary labyrinthine structures. Using an implicit method requires the solution of a large sparsely coupled system of nonlinear equations at each time step. The key to making implicit methods viable is the fast solution of this nonlinear system.

Section 4.1 describes the discretizations of the spatial operators of Eqs. (1.10). The time integration methods and the schemes for choosing an adaptive time step are detailed in Section 4.2. The iterative method for solving the nonlinear system of equations is shown in Section 4.3.

4.1 Spatial Discretization

The first step in the method of lines approach for PDEs is the discretization of the spatial operators. The model equations can be written as

$$U_t = f(U) + DL(U), \quad (4.1)$$



CHAPTER 4. NUMERICAL METHODS

with the L operator given by $L = \partial^2/\partial x^2$ in one dimension or $L = \nabla^2$ in two dimensions. The vector $\mathbf{U}(x, y, t)$ represents the two components (u, v) , and

$$\mathbf{f}(\mathbf{U}) = \begin{bmatrix} u - u^3 - v \\ \epsilon(u - a_1 v - a_0) \end{bmatrix}. \quad (4.2)$$

The boundary conditions are chosen to be either periodic or Neumann (no-flux). For most physical cases, Neumann boundary conditions are the most appropriate. Consider, for example, a stirred chemical reactor. At the boundaries of the reactor the chemical species are not fixed to have a specific concentration. The chemicals cannot, however, have any flow through the wall of the container. In some cases, mostly when studying regular patterns or traveling waves it is more convenient to use periodic boundary conditions. When the period is large compared with the size of single domain structures, both boundary conditions produce the same qualitative results.

In one dimension, periodic boundary conditions imply that $\mathbf{U}(x + L_x) = \mathbf{U}(x)$, where L_x is the domain size. The Neumann, or no-flux, conditions are implemented as symmetric boundary conditions where all of the odd derivatives are zero at the boundaries, $x = 0$, and $x = L_x$,

$$\begin{aligned} \mathbf{U}_x(0, t) = \mathbf{U}_{xxx}(0, t) = \dots = 0, \\ \mathbf{U}_x(L_x, t) = \mathbf{U}_{xxx}(L_x, t) = \dots = 0. \end{aligned} \quad (4.3)$$

In two dimensions the simulations were carried out on a square grid which adds the following conditions: for the periodic case,

$$\mathbf{U}(x, y + L_y, t) = \mathbf{U}(x, y, t), \quad (4.4)$$

where L_y is the size of the domain in the y direction; for the symmetric case,

$$\begin{aligned} \mathbf{U}_y(x, 0, t) = \mathbf{U}_{yyy}(x, 0, t) = \dots = 0, \\ \mathbf{U}_y(x, L_y, t) = \mathbf{U}_{yyy}(x, L_y, t) = \dots = 0. \end{aligned} \quad (4.5)$$

In one dimension the continuous operators were discretized on a uniform mesh of $N + 1$ points on varying domain sizes. The grid points are labeled by x_i , where $i = 0, 1, \dots, N$. Enough grid points were chosen so the grid spacing satisfied $\Delta x = L_x/(N + 1) \leq 1$ (and similarly for y in two dimensions). This choice ensured, for typical parameters ϵ and δ , that there were at least 6 to 8 points across the narrow front region in u . The simulations were checked with higher grid resolutions. Doubling the number of points occasionally changed the exact location of the front bifurcation but did not qualitatively effect the nature of the patterns.

The function \mathbf{f} was represented at the grid points, x_i , by its value at each location $\mathbf{f}(U_i)$, where $U_i = \mathbf{U}(x_i)$. The operator L was replaced with a discrete operator using either 2nd or 4th order finite difference approximations. In the interior regions of the domain we obtain an approximation for LU accurate to second order by the formula,

$$LU_i = \frac{U_{i+1} - 2U_i + U_{i-1}}{\Delta x^2} + \mathcal{O}(\Delta x^2), \quad (4.6)$$



where Δx is the uniform grid spacing. For a fourth order approximation

$$LU_i = \frac{-U_{i+2} + 16U_{i+1} - 30U_i + 16U_{i-1} - U_{i-2}}{12\Delta x^4} + \mathcal{O}(\Delta x^4). \quad (4.7)$$

The DERMOD package [57] of numerical differentiation routines provided a flexible and reliable tool in programming the derivative approximations using these formulas.

At the boundaries the same formulas were used to compute the derivatives by adding fictitious, or ghost points, outside the computational domain. For $2nd$ order finite difference approximations to the second derivative an extra point is needed beyond each end of the one dimensional computational domain and for $4th$ order approximations two extra points are needed beyond each end. The solution is not integrated forward time on these extra points; they are updated between each time step by filling in the values according to the boundary conditions as follows.

For periodic boundary conditions the solutions at the two ends of the domain are identified, $U_0 = U_N$, and we effectively use a grid of only N points. To use centered difference formulas at the boundaries, x_0 and x_{N-1} , we extend the solution periodically, $U_N = U_0$, $U_{N+1} = U_1$, at the right boundary and $U_{-1} = U_{N-1}$, $U_{-2} = U_{N-2}$, at the left. For symmetric boundary conditions we use $N + 1$ points and reflect the solution about the two boundary points U_0 and U_N . At the right end of the domain this results in $U_{N+1} = U_{N-1}$, $U_{N+2} = U_{N-2}$, and at the left end, $U_{-1} = U_1$, $U_{-2} = U_2$.

In two dimensions the function f was represented in the same way as in one dimension: by taking the value of the function at the local grid point. The two dimensional operator $L = \nabla^2$ was discretized using the nine point cross;

$$LU = \hat{L}_{xx}U + \hat{L}_{yy}U + \mathcal{O}(\Delta x^4, \Delta y^4), \quad (4.8)$$

where \hat{L}_{xx} and \hat{L}_{yy} are the one-dimensional $4th$ order approximations given in Eqn (4.7). Written out in all its gory detail,

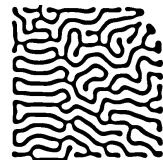
$$\begin{aligned} LU_{i,j} &= \frac{-U_{i+2,j} + 16U_{i+1,j} - 30U_{i,j} + 16U_{i-1,j} - U_{i-2,j}}{12\Delta x^4} \\ &+ \frac{-U_{i,j+2} + 16U_{i,j+1} - 30U_{i,j} + 16U_{i,j-1} - U_{i,j-2}}{12\Delta y^4} \\ &+ \mathcal{O}(\Delta(x^4, y^4)). \end{aligned} \quad (4.9)$$

4.2 Time Integration Methods

After the spatial operators are discretized we are left with a set of coupled ordinary differential equations of the form

$$U_t = F(U, \mathbf{x}, t), \quad (4.10)$$

where F represents the spatially discretized right-hand-side of Eqns. (4.1). We may then use numerical methods for ordinary differential equations to step the solution forward in time. Many



CHAPTER 4. NUMERICAL METHODS

methods will work but some choices are unsuitable because the time-step is restricted for numerical stability of the full discretized PDE solution.

For one-dimensional simulations we used the ODE solver package SDRIV to integrate the coupled system of Eqs. (4.10) [58]. For grid sizes of several hundred points, efficient and fast methods are not crucial since the total computational time is low. The SDRIV package has the capability of utilizing both explicit (the Adams methods) and implicit (Gear) methods. The error is controlled by inputting a tolerance for the absolute and/or relative error per time step. The error is kept under this tolerance by a combination of variable time step and variable method order schemes.

In two dimensions the set of ODE systems to be solved, typically of size 400×400 , required a more efficient code to run in reasonable time on a workstation. For this reason a new code was developed using fixed order methods to save on storage and reduce the computational overhead. Either an explicit or implicit method was used depending on the parameter regime. Because the model equations have second-order spatial derivative terms, numerical stability for explicit methods requires that the time step be bounded by the square of the mesh size. In most cases the grid spacings, Δx and Δy , were $\mathcal{O}(1)$ so the time step was restricted to $\Delta t \sim \mathcal{O}(1)$. For the computations where the dynamics of the solution are fast, such as traveling waves or spiral waves, the time-step restriction for solution accuracy was much less than $\Delta t \sim \mathcal{O}(1)$, and explicit methods were used. For patterns with long time scale slow dynamics, such as labyrinthine structures or slowly oscillating domains, often the time step restriction for accuracy is much larger than $\mathcal{O}(1)$. In that case an implicit method with a variable time-step scheme was used to remove the stability restriction.

For the explicit method, we used the second-order Adams-Bashforth method with a fixed time step. For a time step of size $h = \Delta t$ the solution of Eq. (4.10) at time-step $n + 1$ is in terms of the solution at the previous two time steps, n and $n - 1$,

$$U_{n+1} = U_n + \frac{3h}{2}F_n - \frac{h}{2}F_{n-1} + \mathcal{O}(h^3), \quad (4.11)$$

where $F_n = F(U_n, \mathbf{x}, t_n)$. To start the integration from the initial conditions we set $F_{-1} = F_0$ and take one time step with the locally second order method

$$U_1 = U_0 + hF_0 + \mathcal{O}(h^2). \quad (4.12)$$

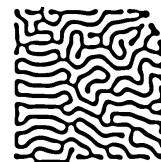
For the implicit method we chose the second order backward differentiation formula (BDF2) [59] which for fixed time-step h is

$$U_{n+1} - \frac{2h}{3}F_{n+1} = \frac{4}{3}U_n - \frac{1}{3}U_{n-1} + \mathcal{O}(h^3). \quad (4.13)$$

Once again to start from the initial $t = 0$ solution, we take a single step, (in this case Backward Euler),

$$U_1 - hF_1 = U_0 + \mathcal{O}(h^2). \quad (4.14)$$

The removal of the stability restriction doesn't come for free. The solution of the discretized equations is now given by a set of implicit nonlinear equations that must be solved at each time step. These equations are solved by a multi-iteration Newton scheme where the nonlinear problem is



CHAPTER 4. NUMERICAL METHODS

linearized (the outer iteration) leaving the resulting linear problem to be solved (the inner iteration). The method for the solution of the nonlinear problem is described in the next section.

Since the main advantage of the implicit method is to remove the stability time-step restriction, we want to be able to take large time steps when the solution has slow dynamics. One method is to stop the simulation, change the time step and restart. A better way is to implement a dynamically adaptive time-step scheme. To do that we need the following pieces: a BDF2 formula for nonuniform time spacings, a method for measuring the solution error at each time step, and a method for picking the size for the next step.

The variable step BDF2 formula is

$$U_{n+1} - \alpha F_{n+1} = \beta_0 U_n - \beta_1 U_{n-1} + \mathcal{O}(r^3). \quad (4.15)$$

The coefficients are

$$\alpha = \frac{2r + s}{r(r + s)}, \quad \beta_0 = \frac{(r + s)^2}{(2r + s)s}, \quad \beta_1 = \frac{r^2}{(2r + s)s}, \quad (4.16)$$

where $r = t_{n+1} - t_n$ and $s = t_n - t_{n-1}$ are the sizes of the current and previous time steps.

The local error at the new time is estimated by comparing the solution, U_{n+1} , with a predicted solution. We used a linear predictor to get an estimate of the solution at the next time-step,

$$U_{n+1}^p = \gamma_0 U_n - \gamma_1 U_{n-1} + \mathcal{O}(h^2). \quad (4.17)$$

The coefficients are $\gamma_0 = (r + s)/s$ and $\gamma_1 = r/s$ which for a fixed time step of size h reduce to the familiar values, $\gamma_0 = 2$ and $\gamma_1 = 1$. The absolute error between the predictor and the corrected solution is measured by taking the scaled norm of the difference,

$$A_{n+1} = \|U_{n+1} - U_{n+1}^p\|. \quad (4.18)$$

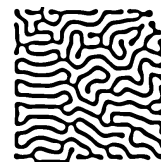
In this case, $\|\cdot\|$ represents the norm

$$\|U\| = (\Delta x \Delta y \sum_{ij} |U_{ij}|^2)^{1/2}, \quad (4.19)$$

where Δx and Δy are the grid spacings in the x and y directions. The relative error is found by scaling with the solution size,

$$R_{n+1} = \frac{A_{n+1}}{\|U_{n+1}\|}. \quad (4.20)$$

The method for selecting a new time step is based on practical experiences developing ODE codes [60]. It is not difficult to estimate time step needed to keep the error per unit step under a given tolerance. The difficulty arises in keeping the time step from oscillating or varying radically over short times. The first step is to make an estimate for the new step size necessary to keep the error under a given tolerance. This new time step is then limited depending on its size and whether the previous time step was successful or not. Since the predictor, U_{n+1}^p , has a leading error of $\mathcal{O}(\Delta t^2)$ and the leading order of the corrector, U_{n+1} , is $\mathcal{O}(\Delta t^3)$, the relative error, R_{n+1} is proportional to



Δt^2 . Given an error tolerance per unit time step, ε , we chose the next time step conservatively and require the relative error 1/2 of the desired input error tolerance

$$\sigma = \frac{\Delta t_{new}}{\Delta t_{old}} = \left(\frac{\varepsilon}{2R_{n+1}} \right)^{1/2}. \quad (4.21)$$

The suggested ration of the time step change, $\sigma = \Delta t_{new}/\Delta t_{old}$, is then restricted to be within a range of values.

If $R_{n+1} < \varepsilon$, the solution passes the error test, is accepted, and new time step is chosen. If $\sigma > 1$ we can increase the time step. We do so only if $\sigma > 2$, and then set $\Delta t_{new} = 2\Delta t_{old}$. If $\sigma < 1$ the time-step must be decreased. We decrease the time step only if $\sigma < .9$ and not by more than a factor of 1/2.

If $R > \varepsilon$, the solution fails the error test, a smaller time step is chosen, and the step is retaken. The step size is reduced the factor $\max(0.9\sigma, 1/4)$. If the solution failed because either the nonlinear solver or the linear solver failed to converge then the time step is reduced by 1/4 and the step retaken.

4.3 Solution of the Nonlinear System

When using the implicit time integration method, on each time step we must solve the nonlinear system of equations

$$U - \alpha F(U) = G_n, \quad (4.22)$$

where G_n represents the known right hand side of Eqn. (4.15) and $U = U_{n+1}$. The $n + 1$ subscripts will be dropped in this section to avoid notational clutter. We seek an iterative solution to this equation by linearizing $F(U)$ and using Newton's method. With the iteration parameter k the linearization is

$$F(U^{k+1}) = F(U^k) + \frac{\partial F}{\partial U}(U^k)(U^{k+1} - U^k). \quad (4.23)$$

Substituting the linearization in (4.22) we have the iteration scheme

$$U^{k+1} - \alpha \left[F(U^k) + \frac{\partial F}{\partial U}(U^k)(U^{k+1} - U^k) \right] = U_n. \quad (4.24)$$

Rearranging terms and subtracting U^k from each side we get

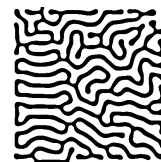
$$\left[I - \alpha \frac{\partial F}{\partial U}(U^k) \right] (U^{k+1} - U^k) = U_n + \alpha F(U^k) - U^k, \quad (4.25)$$

where I represents the identity matrix. If we let

$$A^k = I - \alpha \frac{\partial F}{\partial U}(U^k), \quad (4.26)$$

and define

$$e^{k+1} = U^{k+1} - U^k, \quad (4.27)$$



CHAPTER 4. NUMERICAL METHODS

we are left with the linear system of equations,

$$A^k e^{k+1} = r^k, \quad (4.28)$$

to be solved on each iteration. The residual vector,

$$r^k = U_n + \alpha F(U^k) - U^k, \quad (4.29)$$

is the right hand side of Eqn. (4.25). We iterate on k until the norm of the residual, $\|r^k\|$, is smaller than some given relative error tolerance.

In practice a modified Newton iteration was used. Since the evaluation of the Jacobian, $J^k = \frac{\partial F}{\partial U}(U^k)$, can be computationally expensive we instead fix $J^k = J^0$. Obviously if the solution makes large changes during the iteration this approximation will be bad and the iteration may fail to converge. Whenever two or more iterations are taken we estimate the convergence rate [61],

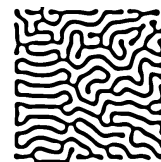
$$\rho = \left(\frac{\|U^{k+1} - U^k\|}{\|U^1 - U^0\|} \right)^{1/k}. \quad (4.30)$$

If $\rho > 0.9$ or more than *MAXITER* iterations have been taken, the iteration is considered to have failed, the time-step is reduced by 1/4, and a new step is taken. Typically the maximum number of iterations allowed was 4.

The steps to implement this method are as follows:

- Step 1: Select an initial guess for $U^{k=0}$. We use the linear predictor (Eqn. (4.17)) and set $U^0 = U^p$
- Step 2: Evaluate $J = \frac{\partial F}{\partial U}(U^0)$
- Step 3: Evaluate the function $F(U^k)$
- Step 4: Compute the residual $r^k = u_n + \alpha F(U^k) - U^k$
- Step 5: Check if $\|r^k\| < \varepsilon_n$. If true the iteration is converged.
- Step 6: Solve $[I - \alpha J(U^k)] e^{k+1} = r^k$
- Step 7: Update the solution, $U^{k+1} = U^k + e^{k+1}$
- Step 8: Estimate the convergence rate, $\rho = \left(\frac{\|U^{k+1} - U^k\|}{\|U^1 - U^0\|} \right)^{1/k}$
- Step 9: If $k > \text{MAXITER}$ or $\rho > 0.9$ the iteration fails. If not set $k = k + 1$, and go to Step 3

The error tolerance for the residual was chosen as $\varepsilon_n = \varepsilon/3$. The reasons for choosing the factor 1/3 are deep and mysterious [61, 62]. Since the iteration is terminated based on the norm of the *residual* and not the solution difference, e^{k+1} , this factor gives an extra margin to ensure that the integrator error estimates are not polluted by the iteration error.



CHAPTER 4. NUMERICAL METHODS

For the most efficient code a specialized solver for the linear system,

$$A^k e^{k+1} = r^k, \quad (4.31)$$

would need to be coded, but we solved it instead by an iterative method contained in the software package NSPCG [63]. The package contains a variety preconditioners and acceleration methods and allows for storage of sparse matrices. Based on experiments with many different methods we finally settled on using a incomplete LU preconditioner with zero level fill-in [64] and the GMRES accelerator [65]. The GMRES algorithm is a particular implementation of a Krylov subspace solver for nonsymmetric matrices.

The stopping condition for the linear iteration was modified from one contained in the package. This modification was needed because the NSPCG code is limited to making relative error estimates. Typically the stopping condition would be

$$\frac{\|(s^{k+1})^2\|}{\|(r^{k+1})^2\|} < \zeta, \quad (4.32)$$

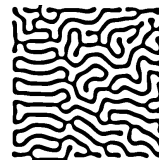
with ζ the input error tolerance and s^{k+1} the residual of the linear system,

$$s^{k+1} = r^k - A^k e^{k+1}. \quad (4.33)$$

The problem is that we are solving for the *difference* of the solution, $e^{k+1} = U^{k+1} - U^k$, and the right-hand-side of the linear system, r^{k+1} , goes to zero. Since we are working in finite precision, when the solution is close to convergence, the error we are measuring using this test is mostly due to roundoff. The code was modified to measure the relative error with respect to the solution size U^k , by the test

$$\frac{\|(s^{k+1})^2\|}{\|(U^{k+1})^2\|} < \zeta, \quad (4.34)$$

where we chose $\zeta = \varepsilon_n/100$, and limited the number if iterations to a maximum of 20.



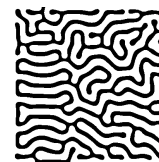
Chapter 5

Conclusion

In this dissertation we have investigated pattern formation in reaction-diffusion systems. We used a simple and well known model to explore different pattern behaviors in one and two dimensions. The approach we took is different than many earlier studies; we focused our analysis on isolated front structures as the basic building blocks of more complex patterns. We found that the number of front solutions depends on the system parameters: at the NIB bifurcation a single stationary Ising front becomes unstable to a pair of counterpropagating Bloch fronts. This multiplicity of fronts allows the formation of traveling patterns. Near the NIB bifurcation the front speed has a multivalued dependence on system perturbations. Perturbations, such as curvature or an external convective field, may induce transitions that reverse the direction of propagating front segments and nucleate spiral-vortex pairs. The nucleation events drive the formation of complex patterns such as spot-splitting and spiral turbulence. The speed vs. curvature relation also shows where planar fronts are unstable and grow to form two-dimensional labyrinthine patterns.

The results in this dissertation are derived for the case of bistable reaction kinetics. Far from equilibrium both Hopf-Turing and excitable systems may show the same behavior. In those cases the system has only one uniform steady state and cannot support isolated fronts. But, far from equilibrium, sharp fronts occur as parts of larger domain structures. These fronts, although not isolated, may also be influenced by the NIB bifurcation. In particular, there may be transitions from stationary patterns far from onset of the Turing instability; on approach to the NIB bifurcation the domains first become unstable to oscillations and then form traveling patterns. Kness *et al.* have studied the bifurcation structure of traveling waves in for the case of $\epsilon \ll 1$ and $\delta = 0$ while varying the reaction kinetics between excitable and bistable scenarios [66].

The NIB bifurcation for the model equations was derived using asymptotic methods and verified numerically in the $\epsilon - \delta$ plane. At the NIB bifurcation the coexistence of front solutions is responsible for the formation of traveling patterns. In the Ising regime there are only single front structures that combine to form, in one dimension, either stationary or oscillating domains but never traveling pulses. If δ is small, fronts propagating in opposite directions annihilate each other and the system goes to the uniform up or down state. Beyond the NIB bifurcation, in the Bloch regime, the multiple fronts combine as a front and a back to form traveling domains. Thus, the NIB front bifurcation indicates where persistent traveling patterns form.



CHAPTER 5. CONCLUSION

One-dimensional oscillating pulses in uniform systems occur in the Ising regime near the NIB bifurcation. This type of oscillation, or breathing motion, was first observed by Koga and Kuramoto in an infinite system [50]. Later Nishiura and Mimura performed an analytic study of oscillations in a finite medium [49]. They found oscillations persisted for parameters well beyond the onset of the breathing motion. We found instead that as we reduce ϵ from the onset of the oscillations, the oscillation amplitude grows until the solution collapses to one of the uniform states. For single domain solutions oscillations never occurred beyond the NIB bifurcation. Oscillations in periodic patterns, however, may be stable in the Bloch regime and coexist with traveling waves [B].

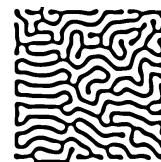
The labyrinthine patterns found in the Ising regime have also been studied by Petrich and Goldstein [67] using a nonlocal interface model. The model was derived for parameters far into the Ising regime where the reaction-diffusion equations reduce to a gradient system. In that regime the equation for the boundary between domains of high and low chemical concentrations leads to a space-filling labyrinthine pattern. We expect the qualitative predictions of that model to hold closer to the NIB bifurcation under two conditions: domain fusion, which changes the topology of the front curve, does not take place, and nongradient effects, such as front transitions, do not appear. It may be possible to modify the interface model to include nongradient effects.

Spot splitting has been studied numerically by Pearson [31, 23] and analytically, in one space dimension, by Reynolds *et al.* [32]. Lee and Swinney also found replicating pulses in one-dimensional simulations of their four variable FIS reaction model [24]. In that case, the parameters of the model were set so the reaction kinetics were monostable. No one-dimensional analog of spot splitting exists in the present model, at least for the parameter regime where splitting in two dimensions has been observed. The splitting studied in this dissertation is a purely two-dimensional effect where curvature and front interactions play key roles. We believe these factors also have important roles in the two-dimensional spot splitting simulations by Pearson.

The breakup of spiral waves results from local front transitions that become feasible near the NIB bifurcation. The transitions can be induced by general perturbations, either extrinsic or intrinsic. In Section 3.6 and [36] we studied front transitions caused by the perturbation of external advective fields. This type of spiral breakup is seen in experiments with the Belousov-Zhabotinski reaction in a thin liquid layer. The target and spiral waves are destroyed by convective motion when the cover of the dish is removed [51, 52].

The transverse instability also can induce local front transitions by creating negatively curved front portions [D]. The geometry of the negatively curved cusp-shaped regions encourages the growth of the inhibiting field and the nucleation of a vortex pair. Another important mechanism for nucleating vortices is the interaction of fronts. Front interactions act directly or indirectly (by flattening curved fronts) to induce transitions. Other studies of spiral wave instabilities have focused on the linear stability and bifurcations of uniformly rotating spiral waves [68, 69]. It would be interesting to investigate the relevance of the front transition mechanisms to those studies and recent studies of spiral turbulence in surface reactions [70] and in cardiac tissue models [71, 72, 73, 74, 75].

Many of the observations made here have also been found in the FIS reaction. These include labyrinthine patterns [22], spot splitting [23], and front transitions induced by front interactions [24]. Further comparative investigation should include experimental testing for the existence of a NIB bifurcation, and examination of the experimental observations in relation to the location of the bifurcation. Measurements of the front velocity near the NIB bifurcations may show a multivalued



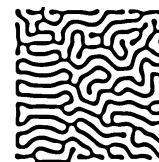
CHAPTER 5. CONCLUSION

speed vs. curvature relation. Current experimental studies are being performed to measure the front speed vs. curvature for isolated chemical spots [76].

We expect similar complex spatio-temporal patterns to be found in other systems exhibiting NIB bifurcations. Periodically forced oscillatory systems [34] and liquid crystals subjected to rotating magnetic fields might be good candidates [77, 78].

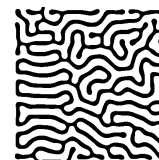
Many open questions still remain. Numerical simulations have shown that front interactions may lead to front repulsion and oscillatory domains. For the oscillating domains in a uniform system [B], a plot of the front speed vs. interfront spacing indicates a transition between the two branches of left and right propagating front solutions. An analysis of front interaction effects on front speeds may provide yet another example of a perturbation that produces a multivalued speed relation. In addition to further understanding the mechanism behind these oscillations, an analysis of the front interactions is necessary to fully describe the complex interactions in the spiral turbulent regimes.

It may be possible to dynamically control patterns using appropriate perturbations near the NIB bifurcation. Since the speed vs. perturbation relation is multivalued there, perturbations such as an external electric field, may cause regular patterns to break. If the perturbation is sufficiently controlled it may provide a way to dynamically nucleate or annihilate spiral waves at specific locations in the system.



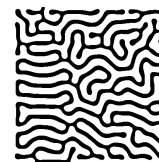
Bibliography

- [1] J. D. Murray, *Mathematical Biology* (Springer, New York, 1990).
- [2] M. C. Cross and P. C. Hohenberg, *Rev. of Mod. Phys.* **65**(3), 2 (1993).
- [3] A. Kolmogorov, I. Petrovsky, and N. Piskunov, *Dokl. Akad. Nauk SSSR* **30**, 301 (1937), reprinted in *Proc. R. Soc. London Ser A* **434** 9 (1990).
- [4] D. G. Aronson and H. F. Weinberger, in J. Goldstein, ed., *Proceedings of the Tulane Program in Partial Differential Equations and Related Topics* (Springer, Berlin, 1975).
- [5] R. Luther, *Z. Elektrochem.* **12**, 596 (1906).
- [6] R. Arnold, K. Showalter, and J. J. Tyson, *J. Chem. Ed.* **64**, 740 (1987).
- [7] R. A. Fisher, *Ann. Eugenics* **7**, 355 (1937).
- [8] A. M. Turing, *Philos. Trans. Roy. Soc. London B* **327**, 37 (1952).
- [9] E. Meron, *Physics Reports* **218**(1), 1 (1992).
- [10] J. J. Tyson and J. P. Keener, *Physica D* **32**, 327 (1988).
- [11] A. Winfree, *When Time Breaks Down* (Princeton University Press, Princeton, NJ, 1987).
- [12] R. FitzHugh, *Biophys. J.* **1**, 445 (1961).
- [13] J. Nagumo, S. Arimoto, and S. Yoshizawa, *Proc. IRE* **50**, 2061 (1962).
- [14] A. C. Scott, *Rev. Mod. Phys.* **47**(2), 487 (1975).
- [15] A. L. Hodgkin and A. F. Huxley, *J. Physiol.* **117**, 500 (1952).
- [16] S. L. McCall, *Applied Physics Letters* **32**(5), 284 (March 1978).
- [17] A. V. Grigor'yants and I. N. Dyuzhikov, *Sov. Phys. JETP* **74**(5), 784 (1992).
- [18] A. V. Grigor'yants and I. N. Dyuzhikov, *J. Mod. Opt.* **37**(4), 597 (1990).
- [19] A. V. Grigor'yants, *Sov. Phys. Solid State* **32**(3), 537 (1990).



BIBLIOGRAPHY

- [20] M. Lax, *Physical Review A* **11**(4), 1365 (1975).
- [21] H. Haug and S. W. Koch, *Quantum Theory of the Optical and Electron Properties of Semiconductors* (World Scientific Publishing Co. Ptc. Ltd., Singapore, 1990).
- [22] K. J. Lee, W. D. McCormick, Q. Ouyang, and H. L. Swinney, *Science* **261**, 192 (1993).
- [23] K. J. Lee, W. D. McCormick, H. L. Swinney, and J. E. Pearson, *Nature* **369**, 215 (May 1994).
- [24] K. J. Lee and H. L. Swinney (1994), "Lammellar structures and self-replicating spots in a reaction-diffusion system." Submitted to *Phys. Rev. E*.
- [25] E. C. Edblom, L. Gyorgyi, and I. R. Epstein, *J. Am. Chem. Soc.* **109**, 4876 (1987).
- [26] V. Gáspár and K. Showalter, *J. Am Chem. Soc* **109**, 4896 (1987).
- [27] V. Gáspár and K. Showalter, *J. Phys. Chem.* **94**, 4973 (1990).
- [28] P. Gray and S. K. Scott, *Chem. Eng. Sci.* **38**, 29 (1983).
- [29] P. Gray and S. K. Scott, *Ber. Bunsenges. Phys. Chem.* **90**, 985 (1986).
- [30] B. Peng, V. Gáspár, and K. Showalter, *Phil. Trans. Soc. London A* **337**, 275 (1991).
- [31] J. E. Pearson, *Science* **261**, 189 (July 1993).
- [32] W. N. Reynolds, J. E. Pearson, and S. Ponce-Dawson, *Phys. Rev. Lett.* **72**(17), 2797 (1994).
- [33] A. S. Mikhailov, V. A. Davydov, and V. S. Zykov, *Physica D* **70**, 1 (1994).
- [34] P. Couillet, J. Lega, B. Houchmanzadeh, and J. Lajzerowicz, *Phys. Rev. Lett.* **65**, 1352 (1990).
- [35] J. Lajzerowicz and J. J. Niez, *J. Phys. (Paris) Lett.* **40**, L185 (1979).
- [36] A. Hagberg and E. Meron, *Phys. Rev. Lett.* **72**(15), 2494 (1994), <http://math.lanl.gov/People/aric/Papers/turb/>.
- [37] By a "gradient" system we mean a system whose time evolution is dictated by the minimization of a free energy or a Liapunov functional.
- [38] S. P. Dawson, A. Lawniczak, and R. Kapral, *J. Chem Phys.* **100**, 5211 (1994).
- [39] M. Seul, L. R. Monar, L. O'Gorman, and R. Wolfe, *Science* **254**, 1616 (1991).
- [40] R. E. Rosensweig, *Ferrohydrodynamics* (Cambridge University Press, Cambridge, U. K., 1985).
- [41] C. S. Henkee, E. L. Thomas, and L. J. Fetters, *J. Mater. Sci.* **23**, 1685 (1988).
- [42] T. A. Witten, *Physics Today* **43**, 21 (1990).



BIBLIOGRAPHY

- [43] W. W. Mullins and R. F. Sekerka, *J. Appl. Phys.* **35**, 444 (1964).
- [44] D. A. Kessler and H. Levine, *Phys. Rev. A* **41**, 5418 (1990).
- [45] T. Ohta, M. Mimura, and R. Kobayashi, *Physica D* **34**, 115 (1989).
- [46] D. Horváth, V. Petrov, S. K. Scott, and K. Schowalter, *J. Chem. Phys.* **98**(8), 6332 (1993).
- [47] A. S. Mikhailov and V. S. Zykov, *Physica D* **52**, 379 (1991).
- [48] J. Sneyd and A. Atri, *Physica D* **65**, 365 (1993).
- [49] Y. Nishiura and M. Mimura, *SIAM J. Appl. Math.* **49**(8), 481 (1989).
- [50] S. Koga and Y. Kuramoto, *Prog. Theor. Phys.* **63**, 106 (1980).
- [51] K. I. Agladze, V. I. Krinsky, and A. M. Pertsov, *Nature* **308**, 834 (1984).
- [52] S. C. Müller, T. Plesser, and B. Hess, in M. G. Velarde, ed., *Physiochemical Hydrodynamics: Interfacial Phenomena* (Plenum Press, New York, 1988).
- [53] S. Schmidt and P. Ortoleva, *J. Chem Phys.* **67**, 3771 (1977).
- [54] O. Steinbock, J. Schütze, and S. C. Müller, *Phys. Rev. Lett.* **68**(2), 248 (January 1992).
- [55] J. M. Hyman, Tech. rep., Courant Institute of Mathematical Sciences (1976), “C00-3077-139”.
- [56] J. M. Hyman, Tech. rep., Los Alamos National Laboratory (1989), “LA-UR 89-3136”.
- [57] J. M. Hyman and B. Larrouturou, in J. F. Thompson, ed., *Numerical Grid Generation For Numerical Solution of Partial Differential Equations* (Elsevier North-Holland, New York, 1982), p. 487.
- [58] D. Kahaner, C. Moler, and S. Nash, *Numerical Methods and Software* (Prentice Hall, Englewood Cliffs, NJ, 1989).
- [59] C. W. Gear, *Numerical Initial Value Problems in Ordinary Differential Equations* (Prentice Hall, Englewood Cliffs, NJ, 1985).
- [60] L. F. Shampine and M. K. Gordon, *Computer Solution of Ordinary Differential Equations* (W. H. Freeman and Co., San Francisco, 1975).
- [61] K. E. Brenan, S. L. Campbell, and L. R. Petzold, *Numerical Solution of Initial-Value Problems in Differential-Algebraic Equations* (North Holland, Amsterdam, 1989).
- [62] L. F. Shampine, *SIAM J. Sci. Stat.* **1**, 103 (1980).
- [63] T. C. Oppe, W. D. Joubert, and D. R. Kincaid, *NSPCG User’s Guide*, Center for Numerical Analysis, The University of Texas at Austin (April 1988), version 1.0.

-
- [64] G. Dahlquist and Å. Björk, *Numerical Methods* (Prentice Hall, Englewood Cliffs, NJ, 1974).
- [65] Y. Saad and M. H. Schultz, *SIAM J. Sci. Stat. Comp.* **7**(3), 103 (1986).
- [66] M. Kness, L. Tuckerman, and D. Barkley, *Phys. Rev. A* **46**(8), 5054 (October 1992).
- [67] D. M. Petrich and R. E. Goldstein, *Phys. Rev. Lett.* **72**(7), 1120 (1994).
- [68] D. Barkley, *Phys. Rev. Lett.* **68**(13), 2090 (March 1992).
- [69] D. Barkley, *Phys. Rev. Lett.* **72**(1), 164 (January 1994).
- [70] M. Bär and M. Eiswirth, *Phys. Rev. E* **48**, 1635 (1993).
- [71] M. Courtemanche and A. T. Winfree, *Int. J. Bifurcation and Chaos* **1**, 431 (1991).
- [72] A. V. Holden and A. V. Panfilov, *Int. J. Bifurcation and Chaos* **1**, 219 (1991).
- [73] A. Karma, *Phys. Rev. Lett.* **71**, 1103 (1993).
- [74] M. Gerhardt, H. Schuster, and J. J. Tyson, *Science* **247**, 1563 (1990).
- [75] H. Ito and L. Glass, *Phys. Rev. Lett.* **66**, 671 (1991).
- [76] H. L. Swinney, private communication, October 1994.
- [77] T. Frisch, S. Rica, P. Couillet, and J. M. Gilli, *Phys. Rev. Lett.* **72**(10), 1471 (1994).
- [78] K. B. Migler and R. B. Meyer, *Physica D* **71**, 412 (1994).
- [79] A. Hagberg and E. Meron, *Phys. Rev. E* **48**, 705 (1993), <http://math.lanl.gov/People/aric/Papers/domain/>.
- [80] A. Hagberg and E. Meron, *Nonlinearity* **7**, 805 (1994), <http://math.lanl.gov/People/aric/Papers/frontbif/>.
- [81] Y. A. Rzanov, H. Richardson, A. A. Hagberg, and J. V. Moloney, *Phys. Rev. A* **47**(2), 1480 (1993), <http://math.lanl.gov/People/aric/Papers/etalon>.

Appendix A

Domain Walls in Nonequilibrium Systems and the Emergence of Persistent Patterns

The material for this Appendix is found in Ref. [79].

Appendix B

Pattern Formation in Dissipative Nonvariational Systems: The Effects of Front Bifurcations

The material for this Appendix is found in Ref. [80].

Appendix C

Spatiotemporal Oscillations in a Semiconductor Étalon

The material for this Appendix is found in Ref. [81].

Appendix D

From Labyrinthine Patterns to Spiral Turbulence

The material for this Appendix is found in Ref. [36].

Appendix E

Scaling of the Semiconductor Equations

The model equations for the semiconductor resonator as proposed in the original physical variables are

$$\begin{aligned} N_t &= \alpha I(N, T)/\hbar\omega - N/\tau_N + D\nabla^2 N, \\ T_t &= qN/C\rho\tau_N - (T - T_0)/\tau_T + \kappa\nabla^2 T, \end{aligned} \quad (\text{E.1})$$

with the light intensity in the cavity given by

$$I(N, T) = \frac{I_0(1 - R)(1 - e^{-\alpha l})(1 + Re^{-\alpha l})}{(1 - 2Re^{-\alpha l} \cos(4\pi n(N, T)l/\lambda) + R^2e^{-2\alpha l})\alpha l}, \quad (\text{E.2})$$

and the refractive index

$$n(N, T) = n_0 - \sigma N + \gamma T. \quad (\text{E.3})$$

The physical parameters and their typical values are found in Table 1.1.

First scale the independent and dependent variables as follows:

$$\bar{x} = x/L_N, \quad \bar{t} = t/\tau_N, \quad u = N/n_o, \quad v = (T - T_0)/t_o, \quad (\text{E.4})$$

where $L_N = \sqrt{D\tau_N}$, and n_o and t_o are yet to be determined. This produces the system

$$\begin{aligned} u_{\bar{t}} &= \frac{\tau_N I_0}{l\hbar\omega n_o} W(u, v) - u + \nabla^2 u, \\ v_{\bar{t}} &= \frac{qn_o}{C\rho t_o} u - \frac{\tau_N}{\tau_T} v + \frac{\kappa}{D} \nabla^2 v. \end{aligned} \quad (\text{E.5})$$

Assign the new variables $\tau = \tau_T/\tau_N$ and $\delta = \kappa/D$. In the u equation we set

$$\frac{\tau_N}{l\hbar\omega n_o} = 1, \quad (\text{E.6})$$

or

$$n_o = \frac{\tau_N}{l\hbar\omega} \sim 5 \times 10^{14}. \quad (\text{E.7})$$

In the v equation we have

$$\frac{qn_o}{C\rho t_o} = \frac{\tau_N}{lc\rho t_o} = \epsilon \sim 10^{-6}, \quad (\text{E.8})$$

where we choose $t_o \sim 30^\circ K$. Since $1/\tau \sim 10^{-3} \rightarrow 10^{-6}$ let $\tau \rightarrow \epsilon\tau$ (measure τ in units of ϵ).

These scalings leave us with a nondimensionalized version of the model equations where the variables u and v are order one and ϵ is a small parameter.

$$\begin{aligned} u_t &= I_0 W(u, v) - u + \nabla^2 u, \\ v_t &= \epsilon(u - v/\tau) + \delta \nabla^2 v, \end{aligned} \quad (\text{E.9})$$

$$W(u, v) = \frac{(1 - R)(1 - e^{-\alpha l})(1 + R e^{-\alpha l})}{(1 - 2R e^{-\alpha l} \cos(n(u, v)) + R^2 e^{-2\alpha l})}, \quad (\text{E.10})$$

$$n(u, v) = \beta - \beta_N u + \beta_T v, \quad (\text{E.11})$$

For the $W(u, v)$ equation β , β_N , and β_T follow from the scaling of N and T in the original equations.

ϵ - $\tau_N/lc\rho t_o$

τ - cooling time/recombination time

I_0 - input intensity

β - initial refractive index (detuning)

δ - ratio of diffusion coefficients

$\beta_N(> 0)$ - carrier contribution to refractive index index

$\beta_T(> 0)$ - temperature contribution to index